Pergamon

Chaos, Solitons & Fractals Vol. 4, Nos 8/9, pp. 1323–1354, 1994

0960-0779/94$7.00 + .00

0960-0779(94)E0091-3

Pattern Formation in a Passive Kerr Cavity

A. J. SCROGGIE, W. J. FIRTH and G. S. McDONALD*

Department of Physics and Applied Physics, John Anderson Building, Glasgow G4 0NG, UK

and

M. TLIDI and R. LEFEVER

Service de Chimie-Physique, Université Libre Bruxelles, CP 231, Campus Plaine ULB, 1050 Bruxelles, Belgium

and

L. A. LUGIATO

Dipartimento di Fisica, Università di Milano, Via Celoria 16, Milano, Italy

Abstract—Analytic and numerical investigations of a cavity containing a Kerr medium are reported. The mean field equation with plane-wave excitation and diffraction is assumed. Stable hexagons are dominant close to threshold for a self-focusing medium. Bistable switching frustrates pattern formation for a self-defocusing medium. Under appropriate parametric conditions that we identify, there is coexistence of a homogeneous stationary solution, of a hexagonal pattern solution and of a large (in principle infinite) number of localized structure solutions which connect the homogeneous and hexagonal state. Further above threshold, the hexagons show defects, and then break up with apparent turbulence. For Gaussian beam excitation, the different symmetry leads to polygon formation for narrow beams, but quasihexagonal structures appear for broader beams.

1. INTRODUCTION

The phenomena of spontaneous pattern formation and transformation are of general interest for all sciences [1, 2]. Of conceptually fundamental importance are the processes by which a spatial pattern arises from a homogeneous state, as a consequence of the combined action of a nonlinearity and of a cross-talk mechanism among the different spatial points, as for example diffusion. This mechanism was first elucidated in a pioneering work of Turing [3], whence it is customary to call Turing instabilities those instabilities which lead to the onset of a stationary structure from a spatially uniform state.

The last decade has witnessed an increasing interest in the phenomena which arise in the structure of the electromagnetic field in the planes orthogonal to the direction of propagation, when the field travels through a nonlinear medium. These activities have created a new discipline which is commonly designated transverse nonlinear optics [4–6]. In the case of optical systems, diffraction of radiation provides the cross-talk mechanism necessary for spontaneous structure formation.

*Present address: Optics Section, Blackett Laboratory, Imperial College of Science, Technology and Medicine, Prince Consort Road, London SW7 2BZ, UK.

Passive systems without population inversion were the first to be systematically investigated from the viewpoint of transverse pattern dynamics. Moloney *et al.* [7] considered a ring cavity containing a saturable refractive medium, and showed the formation of soliton-like structures on top of the Gaussian profile of the field intensity. In the case of two transverse dimensions, the evolution exhibits the onset of filaments in a ring pattern; the filaments show a slow chaotic dance and then, in the course of a very long time evolution, give rise to the formation of patterns which exhibit a progressive loss of symmetry [8].

Two of us formulated a simple model [9] which demonstrates in a paradigmatic way the existence of a Turing instability in a nonlinear optical system, in a way similar to what is shown by the so called Brusselator [1, 10] in the case of nonlinear chemical reactions. The model is essentially a generalization of the mean-field model for dispersive optical bistability [11] to include diffraction.

Pattern formation in counterpropagating waves in a cavityless Kerr or saturable passive dispersive medium was the subject of intensive investigations in recent years [12–24]. The most prominent phenomenon which emerges in this case is the formation of regular hexagonal patterns, with properties similar to those of hexagonal cellula in the Rayleigh–Bernard instability [25]. These structures have been experimentally observed by Grynberg and collaborators in Na [12] and in Rb [24] and theoretically predicted in refs [13, 17].

The purpose of this paper is to analyse and simulate the model [9] in two transverse dimensions. The advantage of this equation with respect, for example, to the case of counterpropagating waves, is that it involves only two spatial coordinates, and therefore requires much less numerical power. The linear stability analysis of the homogeneous stationary solution was already done in [9]. Here we provide both a detailed bifurcation analysis of the stationary patterns which may be produced by the instability, and an extensive numerical investigation of the stationary and dynamical structures both close to and well beyond the instability threshold. A comparison of analytical and numerical results is also provided. A preliminary account of some of these results was given in [26].

In Section 2 we review the model and the linear stability analysis of the transversally homogeneous stationary solution. Section 3 illustrates the nonlinear bifurcation analysis, the results of which are compared to numerical simulations in the next section. Section 4, in turn, describes hexagonal patterns, of both stationary and chaotic nature. In Section 5 we illustrate the localized structures and the conditions under which one can find them.

All the results in Sections 2–5 are obtained assuming a plane-wave configuration for the input field. In Section 6 we focus, instead, on the case of a Gaussian beam excitation and show that one can recover structures closely related to the hexagonal patterns of the plane-wave case for broad input beams, whereas in the case of narrow beams one meets polygonal structures. The final Section 7 discusses the main results of this paper.

2. THE MODEL

We consider a unidirectional ring (Fig. 1(a)) or Fabry–Perot (Fig. 1(b)) cavity with plane mirrors, containing a Kerr medium and driven by a coherent plane-wave field. Assuming conditions such that only one longitudinal mode of the cavity is relevant, the dynamics of the system can be described by the partial differential equation [9]

$$\frac{\partial E}{\partial \tau} = -E + E_I + i\eta(|E|^2 - \theta)E + ia\nabla_\perp^2 E, \tag{1}$$

where E is the normalized slowly-varying envelope of the electric field, E_I is the

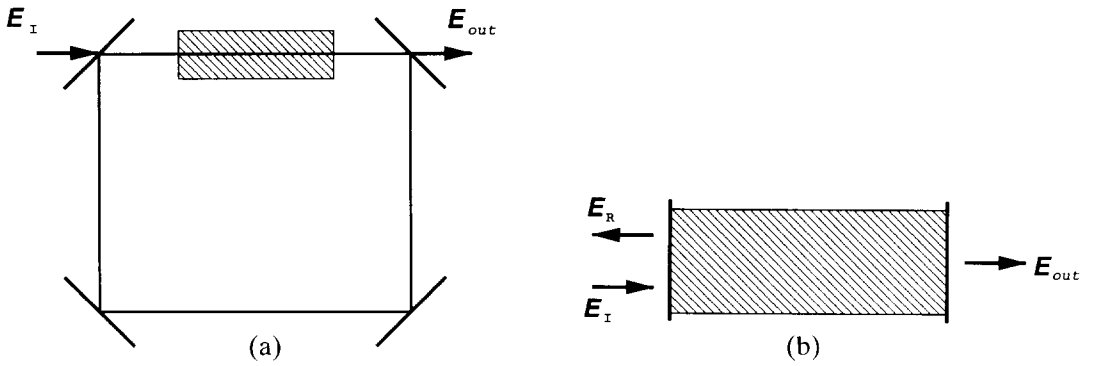

Fig. 1. (a) Ring cavity; (b) Fabry–Perot cavity.

normalized input field (assumed real and positive for definiteness) and θ is the detuning parameter. The normalized time τ is defined as

$$\tau = t/t_{\mathrm{ph}} \tag{2}$$

where t_{ph} is the mean lifetime of photons in the cavity given by L/cT for a unidirectional ring cavity and by $2L/cT$ for a Fabry–Perot cavity, with L being the cavity length, T the transmission coefficient of the cavity mirrors and c the light velocity in vacuum. The parameter η equals $+1$ (-1) for self-focusing (self-defocusing) Kerr media. The transverse Laplacian, which describes diffraction in the paraxial approximation, is given by

$$\nabla_{\perp}^2 = \frac{\partial^2}{\partial x'^2} + \frac{\partial^2}{\partial y'^2}, \qquad x' = x/b, \qquad y' = y/b, \tag{3}$$

where b is an arbitrary length, introduced to make dimensionless the parameter a, which is defined as

$$a = \frac{c\lambda t_{\mathrm{ph}}}{4\pi b^2}; \tag{4}$$

λ denotes the wavelength. By appropriate choice of b, a can always be set to unity.

Equation (1) holds also in the case of cavity containing a two-level medium under conditions of large atomic detuning, as demonstrated in [28].

Both cases of unidirectional ring cavity and Fabry–Perot, under conditions of single-longitudinal-mode operation, lead to the same equation (1), and the difference remains hidden in the normalization constant which links the variable E to the field envelope. An alternative derivation of (1) from the full counterpropagation equations with mirror boundary conditions for a Fabry–Perot cavity, based on a pole analysis, is given in [29].

In [9] the model (1) was analysed in the case of one transverse dimension which can be forced, for example, by introducing a waveguide configuration. In this paper, instead, we will consider the full two-dimensional (2D) model.

Equation (1) admits transversely homogeneous stationary solutions (i.e. solutions independent of time and of the transverse variables x and y) which obey the classic steady-state equation [11]

$$E_I^2 = |E_s|^2[1 + (\theta - |E_s|^2)^2]. \tag{5}$$

The steady-state curve of $|E_S|^2$ as a function of E_I^2 is single-valued for $\theta < \sqrt{3}$ and S-shaped (i.e. exhibits optical bistability) for $\theta > \sqrt{3}$ (Fig. 2(a), (b)). By introducing the transformation

$$E = E_S(1 + A) \tag{6}$$

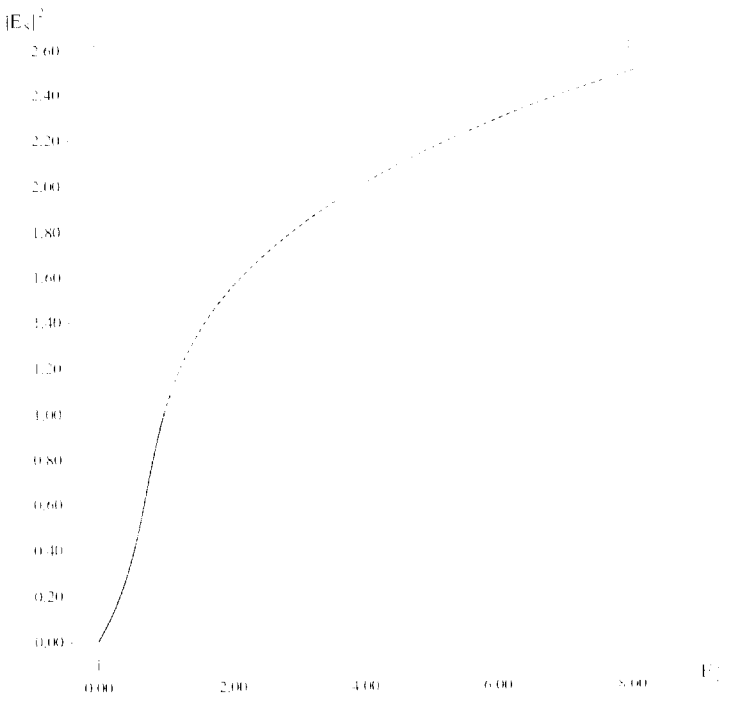

(a)

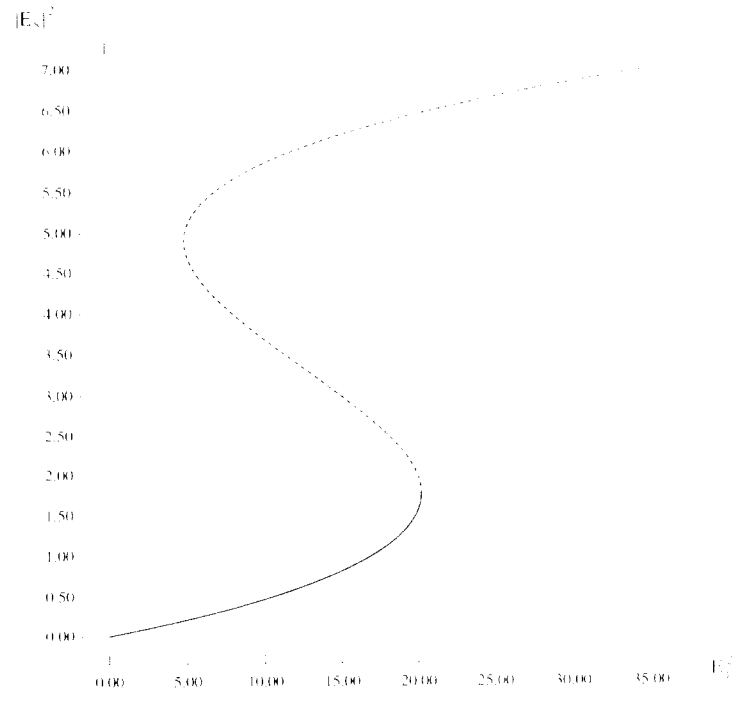

(b)

Fig. 2. Transversally homogeneous stationary solution. The graph shows the stationary intensity $|E_s|^2$ as a function of the input intensity for (a) $\theta = 1$, (b) $\theta = 5$. The dotted parts are unstable in the self-focusing case $\eta = 1$.

equation (1) becomes

$$\frac{\partial A}{\partial \tau} = -[1 + i\eta(\theta - |E_S|^2)]A + ia\nabla_\perp^2 A + i\eta|E_S|^2(A + A^* + A^2 + 2|A|^2 + A|A|^2) \quad (7)$$

and displays quadratically nonlinear terms which typically lead to hexagon formation [31]. Note that (7) is fully equivalent to (1), i.e. there are no additional approximations involved. As well as the quadratic terms responsible for hexagon formation, we can recognize in (7) a phase-conjugate term, and cubically nonlinear terms which saturate the hexagon amplitude.

If we set

$$\theta = |E_S|^2 \quad (8)$$

equation (7) becomes formally identical to a model recently proposed by Courtois and Grynberg [22] to provide an approximate description of the system of counterpropagating waves in a cavityless Kerr medium. With respect to the steady-state equation (5), condition (8) defines the 'bleaching point' where the transmitted intensity equals the input intensity, i.e. $|E_S|^2 = |E_I|^2$. As a matter of fact, in the case of counterpropagating waves in a Kerr medium the field intensity is constant along the sample. For $\theta \neq |E_S|^2$, (7) can be viewed as a generalization of the model [22] to include the possibility of complex values for the damping rate of the field, which is of course a characteristic feature of an optical cavity.

The stability of the stationary solution (5) can be analysed by assuming that A is small and by linearizing (7) with respect to A. The linearized equation must be considered of course, together with its complex conjugate equation to which it is coupled by the phase-conjugate term A^* in (7). Thus, the linearized problem reads

$$\frac{\mathrm{d}}{\mathrm{d}t}\begin{pmatrix} A \\ A^* \end{pmatrix} = L\begin{pmatrix} A \\ A^* \end{pmatrix} \quad (9)$$

where the operator L is given by

$$L = \begin{pmatrix} -[1 + i\eta(\theta - 2|E_S|^2) + ia\nabla_\perp^2 & i\eta|E_S|^2 \\ -i\eta|E_S|^2 & -[1 - i\eta(\theta - 2|E_S|^2) - ia\nabla_\perp^2 \end{pmatrix}. \quad (10)$$

By introducing the ansatz that the perturbation A has the form of a plane-wave modulation

$$\begin{pmatrix} A \\ A^* \end{pmatrix} \alpha e^{\lambda t} e^{i\vec{k}\cdot\vec{x}}, \quad (11)$$

where $\vec{x} \equiv (x, y)$ and $\vec{k} \equiv (k_x, k_y)$, one obtains the characteristic equation for λ which governs the stability. It turns out [9] that the stationary state characterized by the value $|E_S|^2$ is unstable with respect to the growth of modulations with modulus of the transverse wavevector $k = (k_x^2 + k_y^2)^{1/2}$ such that

$$a^{(-)}(|E_S|^2) < ak^2 < a^{(+)}(|E_S|^2), \quad (12)$$

with

$$a^{(\pm)}(|E_S|^2) = \eta(2|E_S|^2 - \theta) \pm (|E_S|^4 - 1)^{1/2}. \quad (13)$$

As shown in [30] this instability is caused by the four-wave mixing process which involves three modes $\vec{k} = 0$ (pump mode), $\vec{k} = \vec{k}_S$ and $\vec{k} = -\vec{k}_S$ (signal modes), where the orientation of the transverse wavevector $\vec{k}_S$ is arbitrary. This feature is similar to the case of counterpropagating waves, in which forward four-wave mixing is a significant factor in the instability [14, 16, 17].

Let us consider now the unstable domain in the plane of the variables $(ak^2, |E_S|^2)$ for fixed values of η and θ. We note that a change of the value of θ produces simply a translation of this figure with respect to ak^2 by a quantity $-\eta\Delta\theta$, where $\Delta\theta$ denotes the variation of θ; in performing the translation, one must keep in mind that the physically meaningful values of ak^2 are non-negative. A significant and helpful corollary is that every plane-wave ($k = 0$) instability is just one member of a family of finite-k instabilities all with the same threshold $|E_S|^2$ but corresponding to different cavity tunings. One would expect, therefore, that for a given tuning the lowest threshold instability will often occur at finite k, i.e. the instability will be of pattern-forming type.

Let us examine first the self-focusing case; Fig. 3 shows the unstable domain for $\eta = 1$, $\theta = 1$ and for $\eta = 1$, $\theta = 5$. The curves display a minimum (point C in Fig. 3) which corresponds to the 'critical point' for the onset of the instabililty; its coordinates are

$$|E_S|_c^2 = 1, \qquad aK_c^2 = 2 - \theta, \tag{14}$$

where K_c depends on the critical value of k. Note that equation (14) only has physical meaning for values of $\theta < 2$. For $\theta = \sqrt{3}$ the point A lies on the vertical axis, and in the bistable case $\theta > \sqrt{3}$ the unstable domain intersects the vertical axis in the segment BD (Fig. 3), which corresponds to the negative slope portion of the steady-state curve (see Fig. 2(b)). For $\sqrt{3} < \theta < 2$ the entire upper branch of the hysteresis cycle (Fig. 2(b)) is unstable as well as a segment of the lower branch, whereas for $\theta > 2$ the upper branch is still unstable but the lower branch is stable.

In the self-defocusing case, the instability exists only for $\theta > 2$, hence only in conditions of bistability, and affects only the segment CD of the lower branch (Fig. 4(a)). Figure 4(b) shows the unstable domain in this case; the critical point C has coordinates

$$|E_S|_c^2 = 1, \qquad ak_c^2 = \theta - 2. \tag{15}$$

Because the upper branch is stable, it is expected that finite wavevector perturbations in

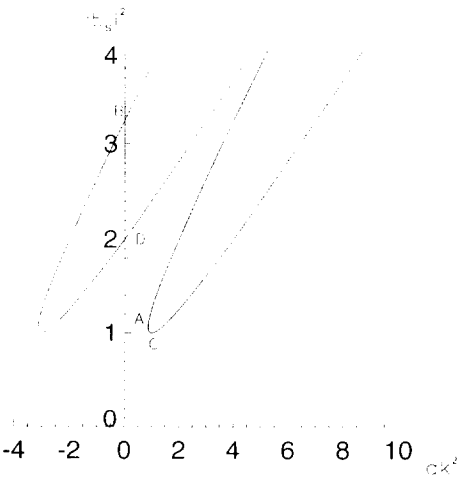

Fig. 3. Self-focusing case $\eta = 1$. The figure shows the domain of the plane $(ak^2, |E_S|^2)$ in which the transversally homogeneous stationary solution is unstable to the growth of inhomogeneous perturbations for $\theta = 1$ (the solid curve) and $\theta = 5$ (the dotted curve). Note that the negative part of the ak^2 axis has no physical meaning and is drawn only to show that the dotted curve is simply a translation of the solid curve parallel to the horizontal axis.

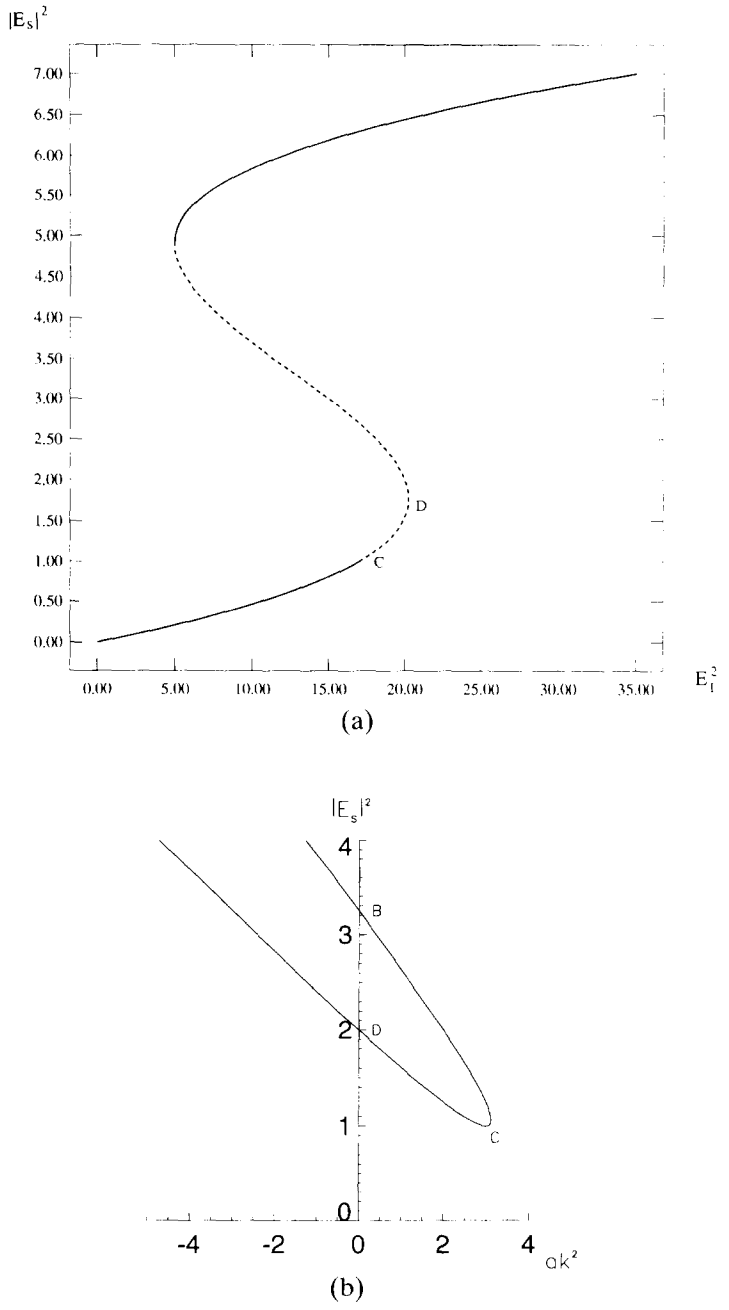

Fig. 4. (a) Same as Fig. 2(b), but the dotted part is unstable in the self-defocusing case $\eta = -1$. The section CD indicates the lower branch instability region. (b) Same as Fig. 3, but for $\eta = -1$, $\theta = 5$.

the instability region of the lower branch will simply cause the system to switch to a plane-wave solution on the upper branch.

The predictions of the linear stability analysis described in this section have been confirmed numerically, for both focusing and defocusing media, and will be discussed in Section 4.

3. NONLINEAR ANALYSIS

The linear stability analysis of the previous section gives information about where the homogeneous, stationary solution of (1) becomes unstable to small perturbations. Once we are above the linear threshold however (given by $|E_S|^2 = 1$), we must turn to some form of nonlinear analysis in order to find out about the behaviour of any non-trivial solution which may emerge from the bifurcation [27].

In the case of one transverse dimension the nonlinear analysis, performed in [9], predicts the bifurcation of a modulated wave; the bifurcation is supercritical for $\theta < 41/30$. In the 2D case, that we analyse in this paper, the nonlinear analysis of the bifurcation of a roll pattern can be performed in a similar way, but we do not report these calculations because in 2D, as we will see, the roll pattern is unstable against the formation of hexagons. In this section we describe two approaches used to find the amplitudes of pure, stationary hexagonal patterns which exist as stable solutions above the linear threshold, primarily as a comparison with out numerical results.

The first method which we consider [22] involves a perturbation expansion of both the amplitude of the field and of $\kappa = |E_S|^2$, which we term the control parameter. Above the bifurcation point the amplitude of any non-trivial solution has a functional dependence on the control parameter. In order to make this dependence explicit both the amplitude and κ are expanded in powers of the same smallness parameter ε [27], which is eliminated at the end of the calculation.

To avoid terms of $O(\varepsilon^0)$ in our calculation we choose to analyse equation (7) which we rewrite in the following form

$$\frac{\partial A}{\partial t} = -(1 + i\delta)A + ia\nabla_1^2 A + i\eta k(A + A^* + A^2 + 2|A|^2 + A^*|A|^2), \tag{16}$$

where $\delta = \eta(\theta - |E_S|^2)$

Writing $\mathbf{V} = [R, I]^T$ where R and I are the real and imaginary parts of the field A, respectively [22], we then have

$$\mathbf{V} = \varepsilon\mathbf{V}^{(1)} + \varepsilon^2\mathbf{V}^{(2)} + \varepsilon^3\mathbf{V}^{(3)} + \ldots, \tag{17}$$

$$\kappa = \kappa_c + \varepsilon\kappa^{(1)} + \varepsilon^2\kappa^{(2)} + \varepsilon^3\kappa^{(3)} + \ldots, \tag{18}$$

with $\kappa_c = 1$.

We assume that our lowest order solution is of the form $\mathbf{V}^{(1)} = \mathbf{v}^{(1)}\vartheta(x, y)$ where ϑ is a function containing the transverse dependence of the field variable A, in this case a hexagonal pattern. Thus we set

$$\vartheta(x, y) = \frac{1}{\sqrt{3}}\left\{\cos(K_c x) + \cos\left[K_c\left(\frac{x}{2} + \frac{\sqrt{3}y}{2}\right)\right] + \cos\left[K_c\left(\frac{-x}{2} + \frac{\sqrt{3}y}{2}\right)\right]\right\}. \tag{19}$$

Written in this form, the function ϑ is a superposition of three rolls of equal amplitudes, the sum of whose phases is zero. This represents a hexagonal pattern of spots consisting of peaks in the intensity. If, instead, we had allowed the sum of the phases of the three rolls to equal π another hexagonal solution would be obtained whose spots are minima of intensity corresponding to a 'honeycomb' structure. Only one of these two patterns is stable, however [31], and in the present case the stable form is always the one we have written in equation (19).

We substitute (17) and (18) into (16) and solve the resulting equation at each order in ε.

At $O(\varepsilon)$ we obtain

$$L\mathbf{V}^{(1)} = \begin{pmatrix} -1 & \delta - a\nabla^2 \\ 2\eta\kappa_c - \delta + a\nabla^2 & -1 \end{pmatrix} \mathbf{V}^{(1)} = 0, \tag{20}$$

which, remembering that $\mathbf{V}^{(1)} = \mathbf{v}^{(1)}\vartheta(x, y)$, has solution

$$\mathbf{V}^{(1)} = \alpha \begin{pmatrix} 1 \\ \eta \end{pmatrix} \vartheta, \tag{21}$$

where α is a real number.

At $O(\varepsilon^2)$ we have an equation of the form

$$L\mathbf{V}^{(2)} = \mathbf{S}^{(2)} \tag{22}$$

where

$$\mathbf{S}^{(2)} = \begin{pmatrix} 2\eta\kappa_c R^{(1)} I^{(1)} \\ -3\eta\kappa_c R^{(1)^2} - \eta\kappa_c I^{(1)^2} - 2\eta\kappa^{(1)} R^{(1)} \end{pmatrix}. \tag{23}$$

The r.h.s. contains terms quadratic in $\mathbf{V}^{(1)}$ as well as linear terms involving the unknown $\kappa^{(1)}$. There are thus source terms with spatial frequencies $k = 0$, K_c, $\sqrt{3}K_c$, $2K_c$ and it is necessary to separate both $\mathbf{S}^{(2)}$ and $\mathbf{V}^{(2)}$ into their different spatial frequencies and solve this problem for each frequency component separately, which is possible because it is linear in $\mathbf{V}^{(2)}$.

For $k^2 = nK_c^2$, $n = 0$, 3, 4 the problem is quite trivial and simply involves the inversion of the linear matrix L with ∇^2 replaced by $-nK_c^2$. When $k^2 = K_c^2$, however, L is singular from the condition imposed at $O(\varepsilon)$. We must therefore invoke the Fredholm Alternative Theorem [22, 27]. This states that the equation

$$L\mathbf{V}^{(2)}{}_{k^2=K_c^2} = \mathbf{S}^{(2)}{}_{k^2=K_c^2} \tag{24}$$

can only be solved if $\mathbf{S}^{(2)}{}_{k^2=K_c^2}$ is orthogonal to the null-space of $L^\dagger$, the adjoint of L. Since in this case L is self-adjoint we have that $\mathbf{S}^{(2)}{}_{k^2=K_c^2}$ must be orthogonal to $\mathbf{V}^{(1)}$. Imposing this condition allows us to fix the value of $\kappa^{(1)}$ which is contained in $\mathbf{S}^{(2)}{}_{k^2=K_c^2}$ and then to solve for $\mathbf{V}^{(2)}{}_{k^2=K_c^2}$:

$$\kappa^{(1)} = \frac{-\alpha}{\sqrt{3}}, \tag{25}$$

$$\mathbf{V}^{(2)}{}_{k^2=K_c^2} = \frac{\alpha^2}{\sqrt{3}} \begin{pmatrix} -1 \\ \eta \end{pmatrix}. \tag{26}$$

Note that we have, for convenience, imposed the further condition that the higher order corrections to $\mathbf{V}^{(1)}$ should be orthogonal to $\mathbf{V}^{(1)}$ itself [27].

The pattern has now been set for calculations at third and higher orders, which are simply repetitions of that at second order with even more spatial frequencies. We can stop at $O(\varepsilon^3)$, however, indeed solving only for the resonant term (that with $k^2 = K_c^2$) in order to determine the value of $\kappa^{(2)}$, since at third order the most important features of the bifurcation have been captured:

$$\kappa^{(2)} = \alpha^2 \left(\frac{20 - 102\eta\delta + 18\delta^2}{27(1 - \eta\delta)^2} \right). \tag{27}$$

If we denote by $\mathbf{V}_H$ the amplitude of the hexagon mode we then have, up to $O(\varepsilon^2)$:

$$\mathbf{V}_H = \varepsilon\alpha \begin{pmatrix} 1 \\ \eta \end{pmatrix} + \frac{\varepsilon^2\alpha^2}{\sqrt{3}} \begin{pmatrix} -1 \\ \eta \end{pmatrix}, \tag{28}$$

$$\kappa - \kappa_c = \frac{-\varepsilon\alpha}{\sqrt{3}} + \varepsilon^2\alpha^2\left(\frac{20 - 102\eta\delta + 18\delta^2}{27(1 - \eta\delta)^2}\right). \tag{29}$$

Equation (29) can be solved for $\varepsilon\alpha$ and the result substituted into equation (28) to give the amplitude of the hexagons as a function of $\kappa - \kappa_c$. When doing this the following point is worth noting. From equations (18) and (29) you see that at threshold ε is given by $\varepsilon = 0$, $-\kappa^{(1)}/\kappa^{(2)}$ where $\kappa^{(1)}$ is fixed and $\kappa^{(2)}$ is a function of δ. If $\kappa^{(2)}$ is too small we may expect that ε (and therefore the amplitude of the hexagons) is large enough on the stable upper branch to contradict the premise of our calculation, namely $\varepsilon \ll 1$. The most we can then expect is that our perturbation calculation will show the correct qualitative behaviour for the hexagon amplitude (see Fig. 7 and Section 4). With these reservations, however, we have an explicit formula for the hexagon amplitude as a function of the control parameters κ, δ, and for either sign η of nonlinearity.

The second approach which has been used [22, 34] is the standard one of converting a partial differential equation into a system of ordinary differential equations by projecting onto an appropriate basis set. In the present case Fourier modes are the natural basis functions to use. Since a partial differential equation will generate an infinite number of ordinary differential equations by this procedure some form of truncation is necessary [22, 34]. Thus we write the field A as

$$A = \sum_{n=0}^{\infty} A_n(\tau)\Phi_n \tag{30}$$

where the Φ_n are the Fourier modes, and keep only Φ_0 and Φ_1, namely the plane-wave term and the hexagon made itself. A_0 is the modification to the homogeneous solution due to the hexagonal pattern and is generally complex.

We separate A_0 and A_1 into real and imaginary parts

$$A_0 = a_0(\tau) + ia_0'(\tau) \tag{31}$$

$$A_1 = a_1(\tau) + ia_1'(\tau) \tag{32}$$

and substitute into equation (16) to obtain four coupled nonlinear ordinary differential equations:

$$\begin{aligned}\dot{a}_0 = {} & -a_0 + \delta a_0' - \eta\kappa\Big(2a_0a_0' + a_1a_1' + a_0'a_0^2 + \frac{1}{2}a_0'a_1^2 \\ & + \frac{1}{2\sqrt{3}}a_1'a_1^2 + a_0a_1a_1' + a_0'^3 + \frac{3}{2}a_0'a_1'^2 + \frac{1}{2\sqrt{3}}a_1'^3\Big)\end{aligned} \tag{33}$$

$$\begin{aligned}\dot{a}_1 = {} & \eta a_1' - a_1 - \eta\kappa\Big(2a_0a_1' + 2a_0'a_1 + \frac{2}{\sqrt{3}}a_1a_1' + \frac{1}{\sqrt{3}}a_0'a_1^2 \\ & + 2a_0'a_0a_1 + a_1'a_0^2 + \frac{5}{4}a_1'a_1^2 + \frac{2}{\sqrt{3}}a_0a_1a_1' \\ & + 3a_0'^2a_1' + \sqrt{3}a_0'a_1'^2 + \frac{5}{4}a_1'^3\Big)\end{aligned} \tag{34}$$

$$\begin{aligned}\dot{a}_0' = {} & -a_0' - \delta a_0 + \eta\kappa\Big(2a_0 + 3a_0^2 + \frac{3}{2}a_1^2 + a_0'^2 \\ & + \frac{1}{2}a_1'^2 + a_0^3 + \frac{3}{2}a_0a_1^2 + \frac{1}{2\sqrt{3}}a_1^3 \\ & + a_0a_0'^2 + \frac{1}{2}a_0a_1'^2 + a_1a_0'a_1' + \frac{1}{2\sqrt{3}}a_1a_1'^2\Big)\end{aligned} \tag{35}$$

$$\dot{a}_1' = -\eta a_1 - a_1' + \kappa\Big(2a_1 + 6a_0a_1 + \sqrt{3}a_1^2 + 2a_0'a_1' + \frac{1}{\sqrt{3}}a_1'^2 + 3a_0^2a_1 + \sqrt{3}a_0a_1^2 + \frac{5}{4}a_1^3 + 2a_0a_0'a_1' + \frac{1}{\sqrt{3}}a_0a_1'^2 + a_1a_0'^2 + \frac{2}{\sqrt{3}}a_1a_0'a_1' + \frac{5}{4}a_1a_1'^2\Big). \tag{36}$$

Finding the fixed points of this system of equations gives the steady-state amplitude, $|A_1|$, of the hexagon pattern. These fixed points cannot be obtained analytically, with the exception of the trival one corresponding to $A = 0$, and we have therefore used the software package KAOS by Guckenheimer and Kim to integrate equations (33) to (36). The solutions obtained can then be used to plot $|A_1|$ as a function of the control parameter κ.

A comparison of the results produced by both of these methods with the results of numerical integration of the equation is presented in the next section.

4. NUMERICAL SIMULATIONS

We have developed two numerical codes to integrate equations (1) and (16). Both codes integrate the model equation on a square grid with periodic boundary conditions. The first code employs a finite-difference Hopscotch algorithm [32] which splits the numerical grid into even and odd points and alternates explicit and implicit steps on each of the two sets of points. The second code integrates the equation using a split-step method [33]; the operator describing the evolution of the field is split into one part consisting of the transverse Laplacian and another part containing all other terms. The Laplacian part is solved using a Fast Fourier Transform routine while a fourth order Runge–Kutta method is employed to solve the remaining part of the equation. The Hopscotch program ran on a Silicon Graphics 4D/210GTX using grids of 128×128 points while the split-step program was run on a VAX with grids of 64×64 points. Most of the simulations were carried out using the Hopscotch code while, because of the completely different character of the numerical method involved, the split-step code acted as a check. Unless otherwise stated all of the following refers specifically to the Hopscotch program to integrate equation (16).

The length of the computational box was generally chosen to be eight times the critical wavelength λ_c, where $\lambda_c = 2\pi/K_c$ with K_c given by equations (14) or (15). Examples of initial conditions used include a pure roll (modulation of the form $\cos(K_c x)$), a Gaussian and a roll on top of a Gaussian—i.e. a field of the form

$$A = f_0 \cos(K_c x) \exp\left[-\frac{(x^2 + y^2)}{r_0^2}\right] \tag{37}$$

with f_0 a real number—both with or without noise added, and simply noise added to the $A = 0$ solution. The noise used was white noise which was filtered in Fourier space to remove high spatial frequencies. This was done to avoid any numerical problems which could occur as a result of large gradients in the initial field.

We first of all discuss the case of a focusing medium ($\eta = 1$ in equation (1)). Carrying out simulations above the linear threshold and using a Gaussian or a roll on top of a Gaussian as the initial condition, without any noise added, it was found that the Gaussian broke up into a series of concentric rings which further broke up in a collection of spots. These spots formed a pattern with roughly fourfold symmetry which persisted until the end of the simulations, a duration of several thousand time-steps. Adding to the initial

condition small amplitude noise (for example an amplitude of 10^{-3}) allowed the spots to escape the pattern of fourfold symmetry imposed by the numerical grid and form a hexagonal pattern instead, as in Fig. 5 for the case of 7% above threshold and $\delta = 0$.

Above threshold an initial condition consisting of a pure roll went to a stationary roll pattern. Adding some small amplitude noise, however, caused the rolls to destabilize leading to the formation of a hexagonal pattern (Fig. 6). Any other initial conditions which were tried gave only hexagonal patterns. It is clear from these results that, for this system at least, studies in one transverse dimension are inadequate to describe the behaviour which occurs when the second transverse dimension is included.

For the case where $\delta = 0$ Fig. 7 compares the hexagon amplitude as a function of the control parameter κ predicted by each of the analytical techniques in Section 3 with the results obtained by numerical integration of equation (16). The numerical points were obtained by starting at 6% above the linear threshold, waiting for a stationary hexagonal pattern to be reached, and then varying the value of κ to trace out the stable hexagon solution branch.

Figure 7 shows moderate correspondence between the numerics and the perturbation calculation. The reason for this was discussed in Section 3, and is due to the fact that the value of $\kappa^{(2)}$ in equation (18) may become too small. Figure 8, which is a plot of the amplitude of the hexagons as a function of δ for $\kappa = 1.07$, demonstrates this. We see that the perturbation calculation comes closest to the numerical result when $\delta \approx -31/33$.

The amplitudes predicted by the modal expansion calculation do not agree too well quantitatively with the numerical results either, although the qualitative behaviour is correct; in particular the régime of coexistence of the stable hexagon and flat solutions in

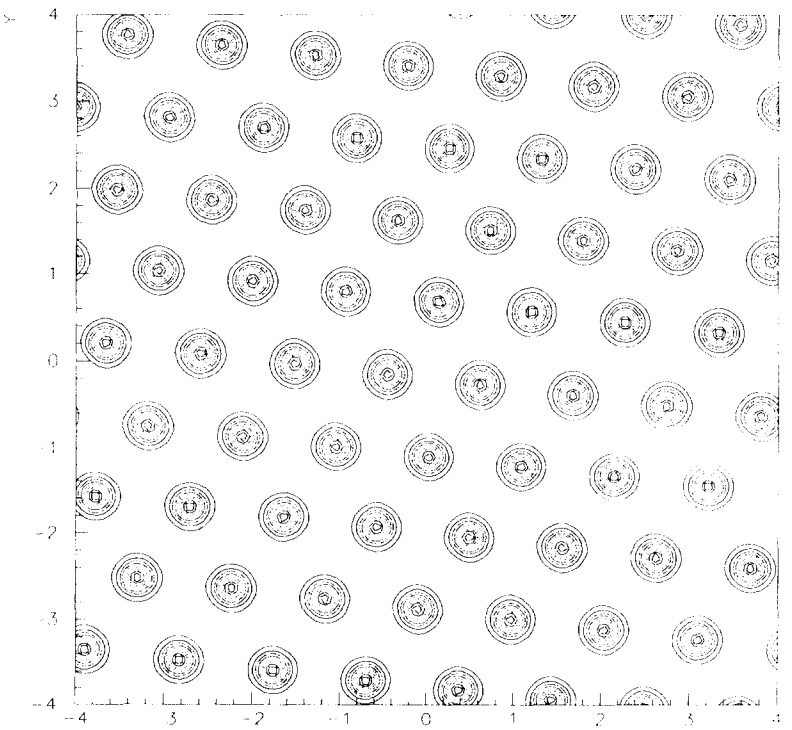

Fig. 5. Contour plot of a stationary hexagon pattern (real part of the field A) in the transverse plane, obtained at 7% above the linear instability threshold ($\kappa = 1.07$). Mean field, $\eta = 1$, $\delta = 0$, $a = 1$ and plane-wave pumping.

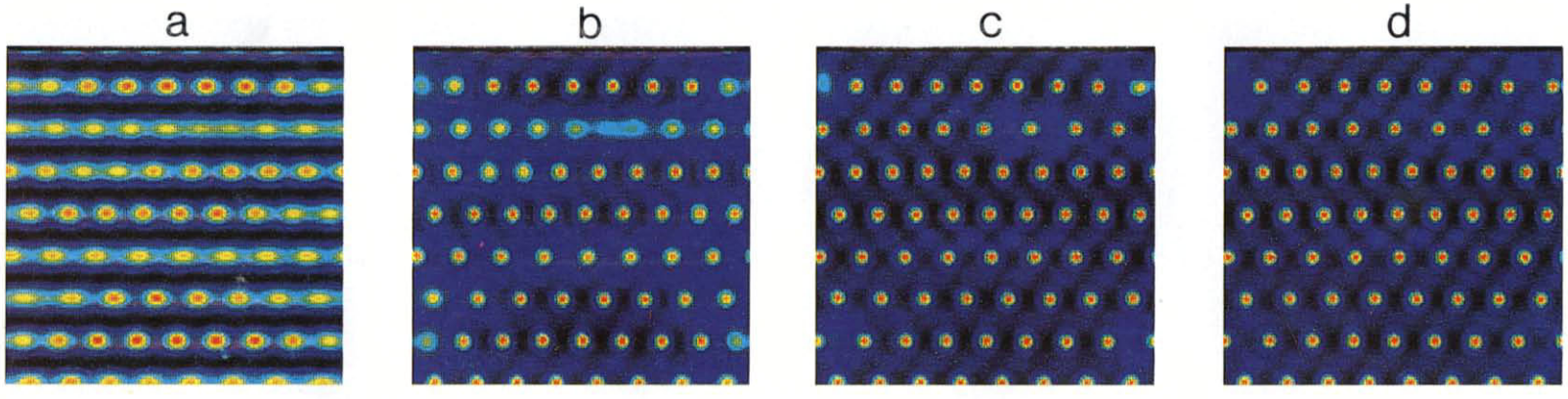

Fig. 6. Time sequence showing the destabilisation of rolls. The initial condition is a roll with small amplitude noise added. The figures show the real part of the field at (a) $t = 18$, (b) $t = 25$, (c) $t = 32$, (d) $t = 39$. The pattern of spots in the final frame undergoes a reorientation on a longer time scale to produce a purely hexagonal pattern. $\eta = 1$, $\delta = 0$, $\kappa = 1.07$, $a = 1$.

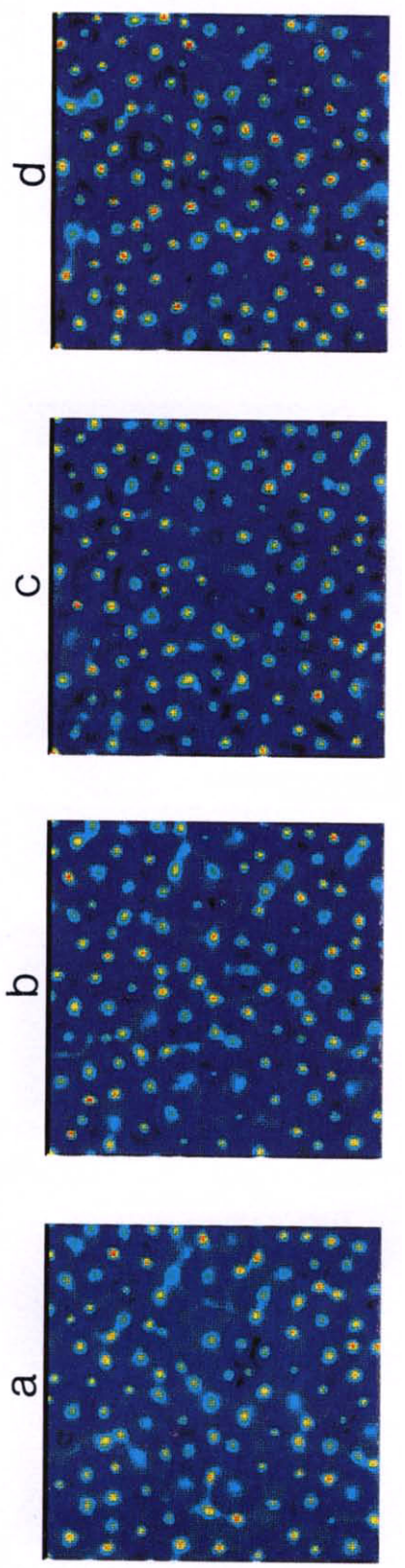

Fig. 10. Time sequence showing turbulent behaviour far above threshold. The figures show the real part of the field at (a) $t = 160.4$, (b) $t = 160.8$, (c) $t = 161.2$, (d) $t = 161.6$, $\kappa = 2.5$, $\delta = -0.65$, $a = 1$ and $\eta = 1$.

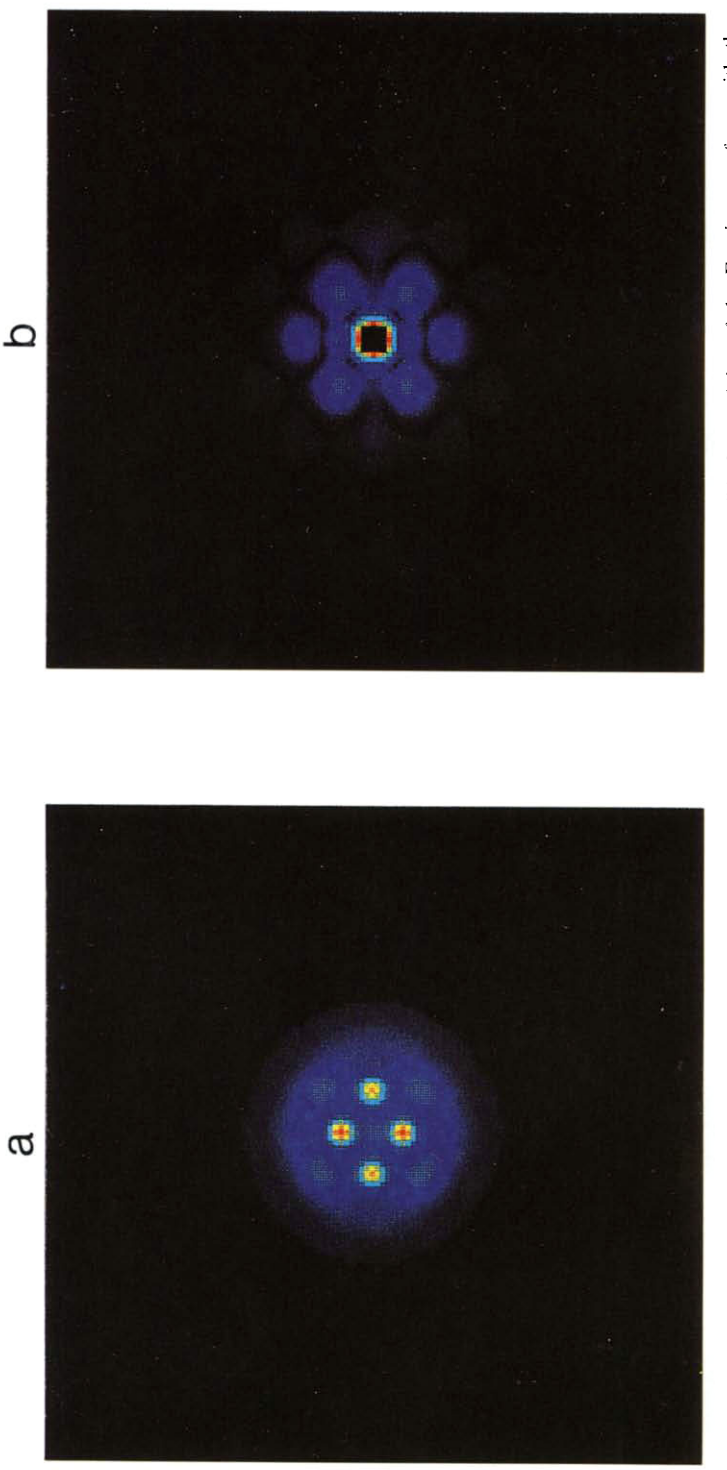

Fig. 15. Gaussian pump. $E_I = 2.5$, $\omega = 5.859$, $\theta = 0$, $a = 1$, $\eta = 1$. (a) The modulus squared of the field; (b) the modulus of the Fourier transform with the central zero-frequency spot removed.

Fig. 16. Gaussian pump. $E_I = 2.5$, $\omega = 4.394$, $\theta = 0$, $a = 1$, $\eta = 1$. (a) The modulus squared of the field: (b) the modulus of the Fourier transform with the central zero-frequency spot removed.

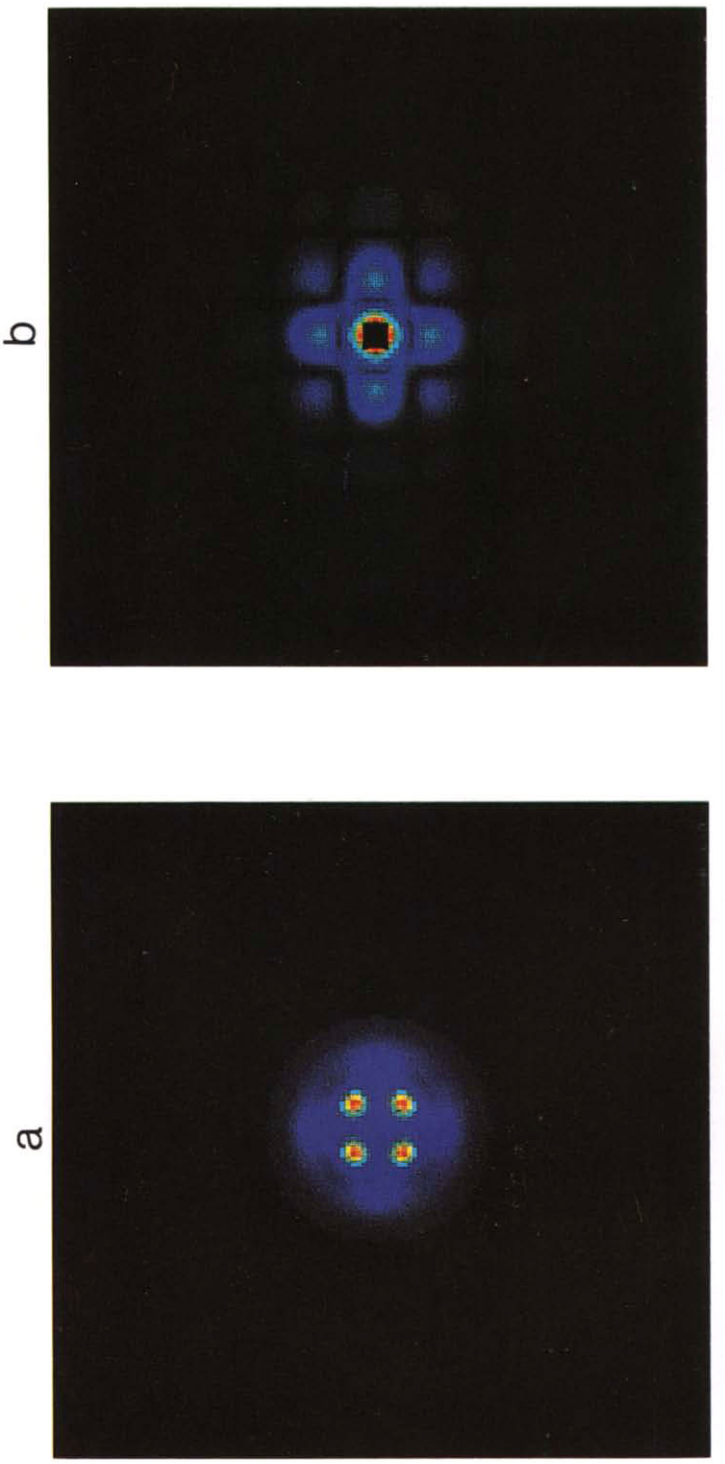

Fig. 17. Gaussian pump. $E_I = 2.5$, $\omega = 5.127$, $\theta = 0$, $a = 1$, $\eta = 1$. (a) The modulus squared of the field; (b) the modulus of the Fourier transform with the central zero-frequency spot removed.

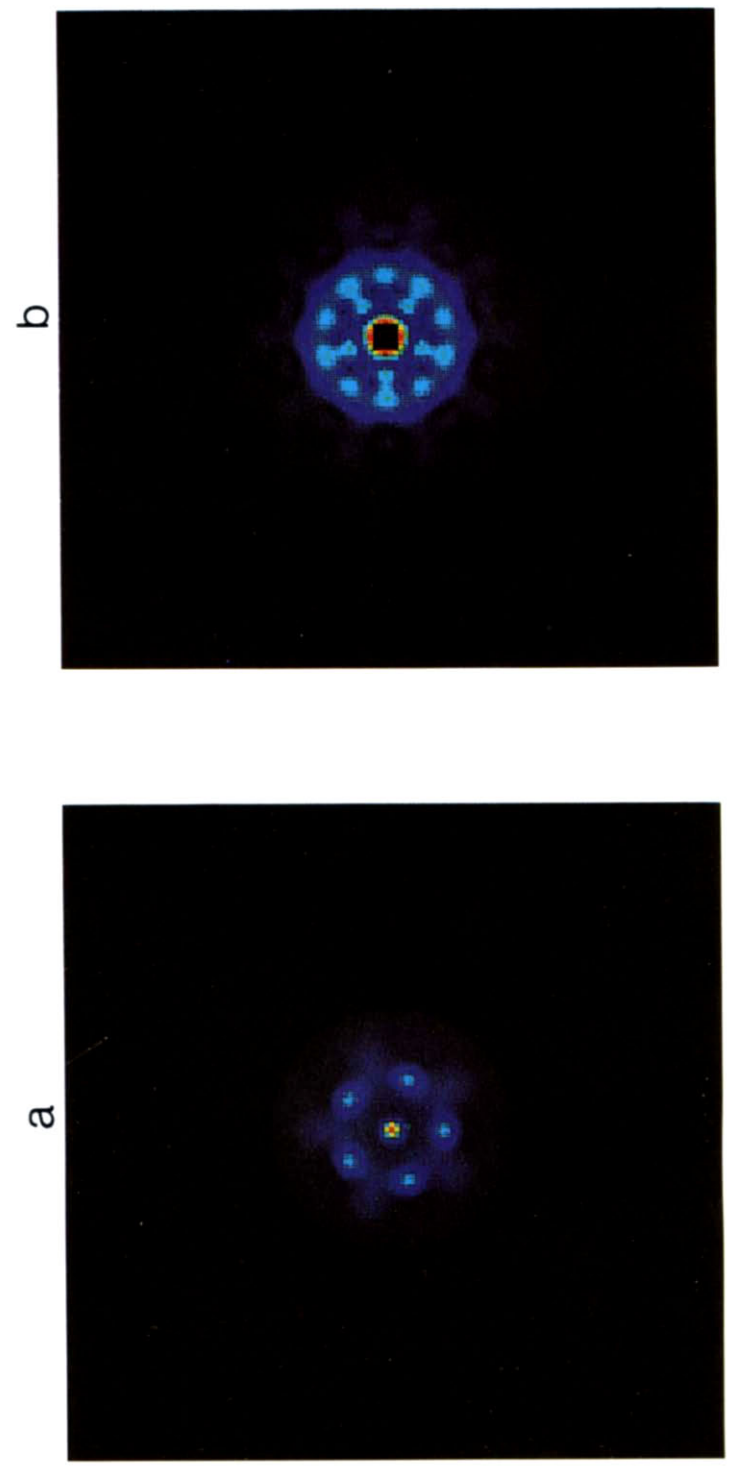

Fig. 18. Gaussian pump, $E_I = 2.6$, $\omega = 5.859$, $\theta = 0$, $a = 1$, $\eta = 1$. (a) The modulus squared of the field; (b) the modulus of the Fourier transform with the central zero-frequency spot removed.

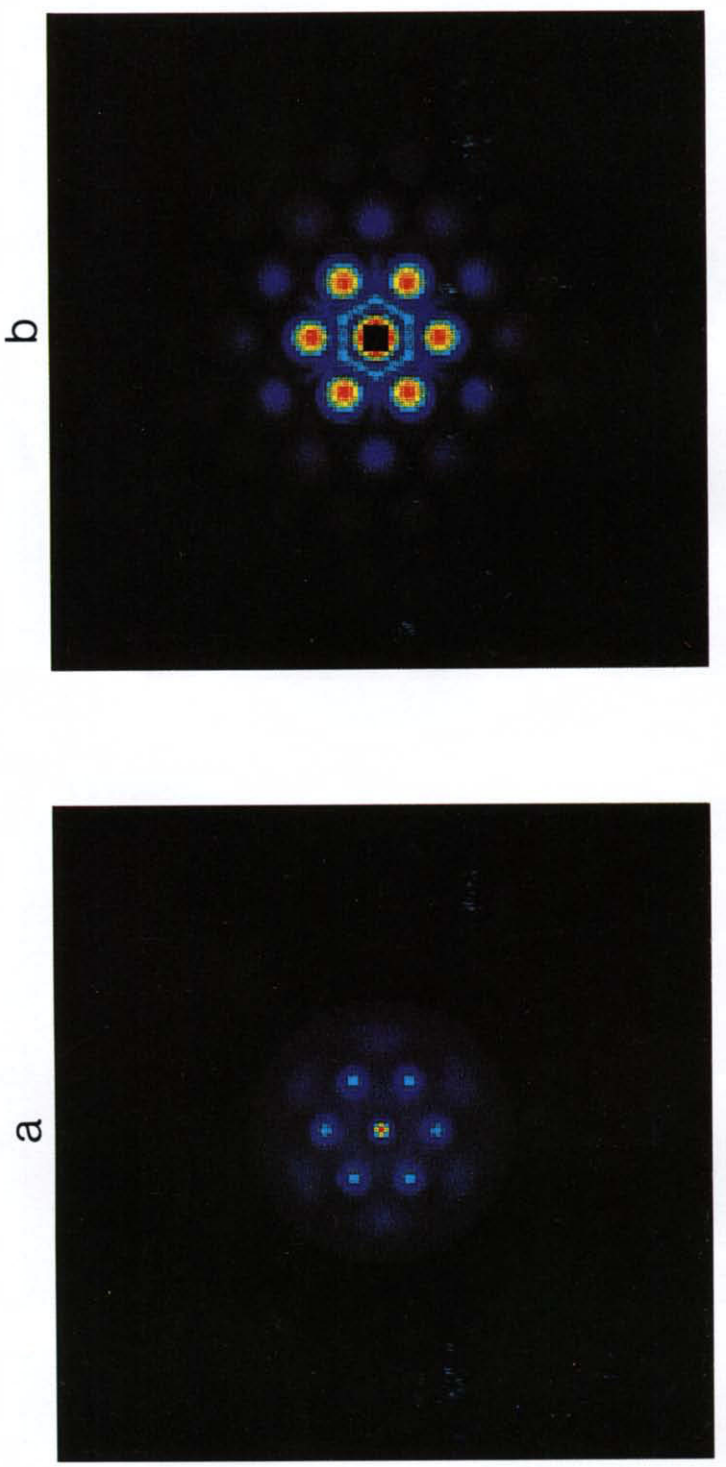

Fig. 19. Gaussian pump. $E_I = 2.6$, $\omega = 6.591$, $\theta = 0$, $a = 1$, $\eta = 1$. (a) The modulus squared of the field; (b) the modulus of the Fourier transform with the central zero-frequency spot removed.

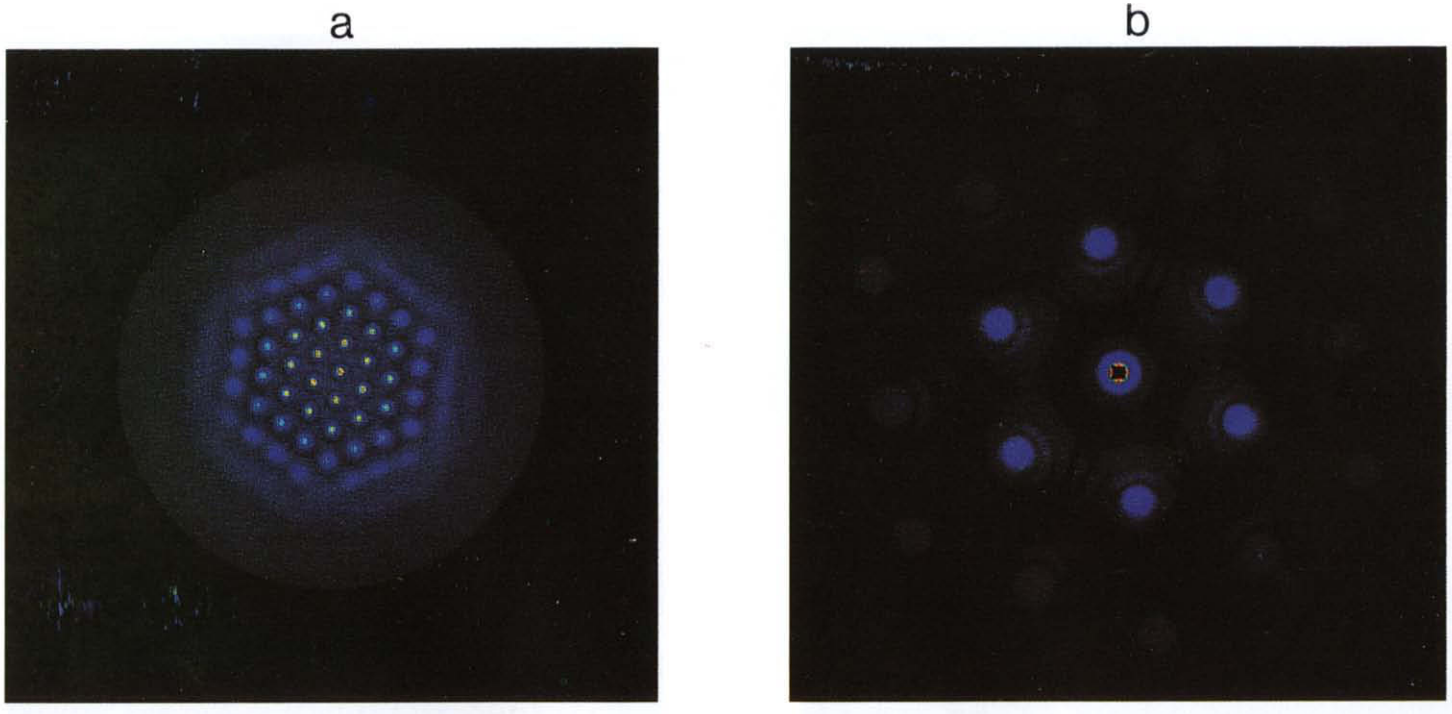

Fig. 20. Gaussian pump, $E_I = 2.1$, $\omega = 21.972$, $\theta = 0$, $a = 1$, $\eta = 1$. (a) The modulus squared of the field; (b) the modulus of the Fourier transform with the central zero-frequency spot removed.

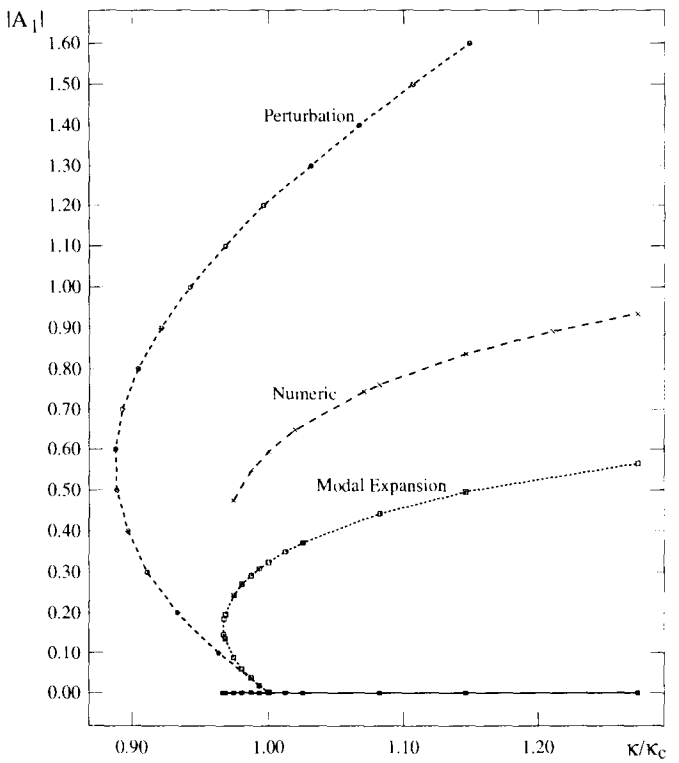

Fig. 7. Comparison of the amplitude of the hexagon pattern, as given by perturbation and modal expansion calculations and by numerical integration, for the case $\delta = 0$, $a = 1$, $\eta = 1$.

Fig. 7, as given by the modal expansion calculation, extends about 3% below the linear threshold, which agrees quite well with the numerics.

Defected patterns can be produced by starting the simulations from noise further above the linear threshold, as in Fig. 9 which shows a penta–hepta defect obtained at 27% above threshold. Such defects persist throughout the length of the simulation, which is typically several thousand cavity lifetimes. Decreasing the control parameter κ causes them to anneal to produce a hexagonal pattern.

All simulations described so far were obtained in the case that the steady-state equation admits only one solution (Fig. 2(a)). When we investigated the case of S-shaped steady-state curve (corresponding to $\theta > \sqrt{3}$ in equations (1) and (5)) it was found that in simulations started on the negative-slope portion of the steady-state curve (Fig. 2(b)) the field appears to switch to the upper stable branch, with the formation of the usual spots in the transverse plane. Recall that for a self-focusing medium part of the negative-slope branch of the bistability curve and the whole of the upper branch (Fig. 2(b)) lie within the region unstable to finite wavevector perturbations.

The search for hexagons on the upper branch is complicated by the fact that, as shown in Section 2, above the linear threshold a continuous band of wavevectors is unstable and the upper branch is far enough above threshold for this to be significant. The problem this presents for numerical simulations is that the size of the numerical grid appears to play a role in the selection of modes: since not all numerical box sizes will accommodate a hexagonal pattern, there appears to be a relationship between the computational box length and the unstable wavevector which, for a given wavevector, allows some box lengths

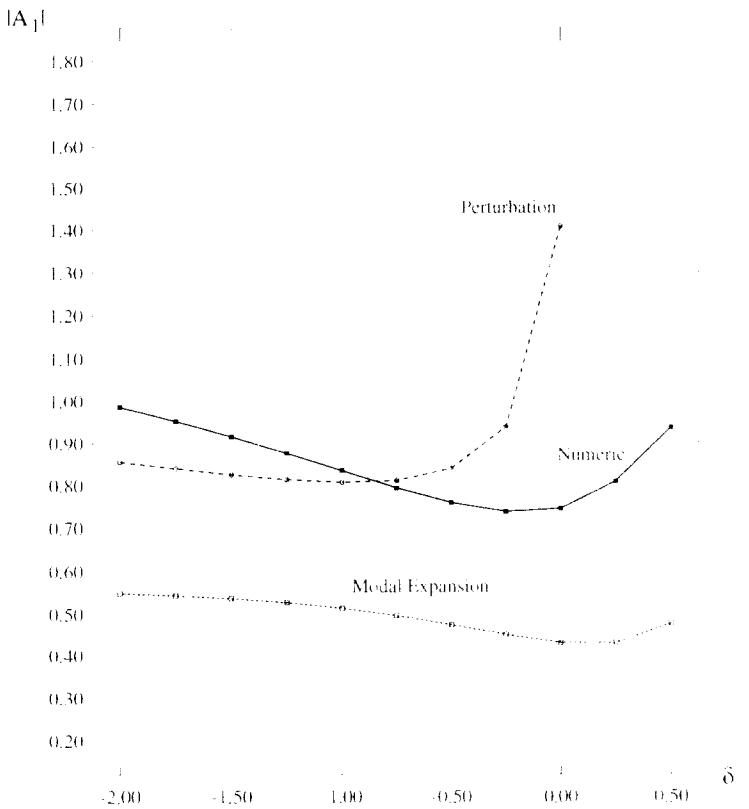

Fig. 8. Comparison of the amplitude of the hexagon pattern as a function of δ for $\kappa = 1.07$, $a = 1$, $\eta = 1$, as given by perturbation and modal expansion calculations and by numerical integration.

and excludes others. The result is that on the order of several tens of percent above threshold it is necessary to try different sizes of computational grid to find the one which produces the optimum hexagonal pattern.

The existence and stability of hexagonal solutions with a wavevector of magnitude K_c on the upper branch were also checked by using a hexagonal pattern as the initial condition and allowing the program to converge to a stable amplitude. This avoids the lengthy box-fitting procedure described above by effectively forcing the solution to have a particular transverse wavevector.

With κ on the order of 150% above threshold and starting from noise, it was found that, instead of the usual stationary patterns, the field exhibited complicated dynamical behaviour with 'spots' appearing, disappearing, moving about and deforming in an apparently disordered way, an example of which is shown in Fig. 10. This far above threshold hexagonal pattern was unstable, breaking up into the kind of turbulent patterns described above. This phenomenon occurred for both monostability ($\theta < \sqrt{3}$) and bistability ($\theta > \sqrt{3}$).

Turning to the case of a defocusing medium (one with $\eta = -1$) we find that from the linear stability analysis of Section 2 such a system is only unstable in the bistable region: specifically for $\theta > 2$ (or $\delta < -1$). In that case the instability region consists of the unstable middle branch of the bistable curve and a small part of the stable lower branch: the stable upper branches entirely outside the instability region. Figure 4(a) shows the bistable curve for the case $\theta = 5$ with the instability region indicated.

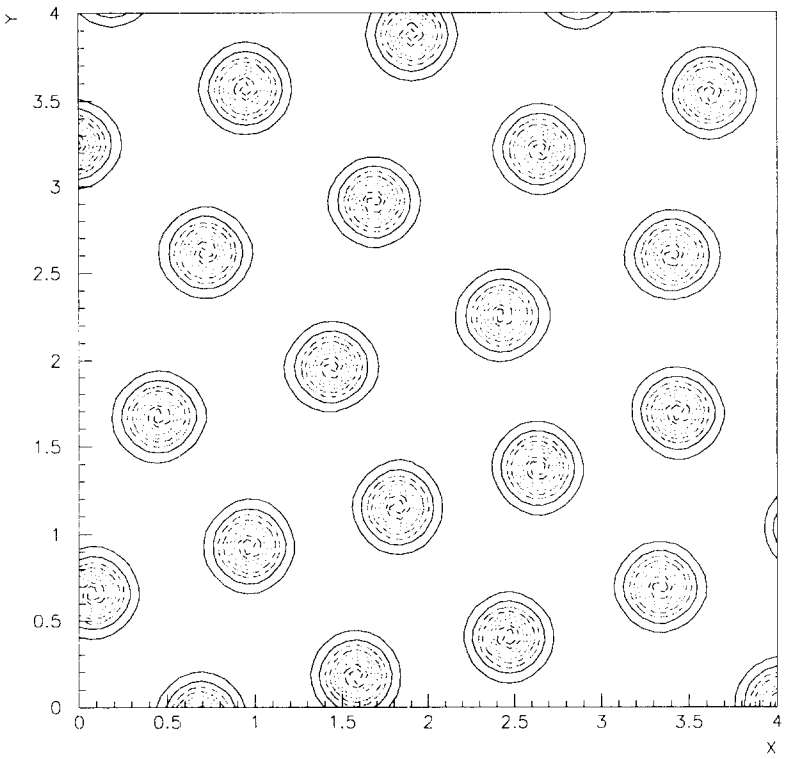

Fig. 9. Penta–hepta defect in the pattern obtained at 27% above threshold, $\kappa = 1.07$, otherwise as Fig. 5. The two spots just right of centre have, respectively, five and seven neighbours.

Simulations carried out for a defocusing medium showed that starting in the finite wavevector instability region, for all the initial conditions tried, the field always switched to the upper branch homogeneous steady-state before any transverse pattern could form. Outside the finite wavevector instability region the behaviour of the field was as expected from plane-wave theory. Thus, no spatial patterns were observable, as expected.

5. LOCALIZED STRUCTURES

Up to this point, we examined hexagonal patterns, either of stationary or of chaotic character. On the other hand, under appropriate parametric conditions, one can meet 2D localized structures instead of patterns. This, was possibly first demonstrated in the case of nonlinear chemical reactions [35] and in hydrodynamics [36]. Recently, the existence of this phenomenon was numerically proved in the case of a 2D optical system, namely a model which describes nascent optical bistability [37, 38]. In this paper, we show that a similar scenario occurs in the paradigmatic optical bistability model given by equation (1). The discussion of this subject requires a digression to the 1D case. The numerical simulations in both the 1D case and in the 2D case have been performed using periodic boundary conditions. A first algorithm was based on the implicit method [39]. In the case of 1D simulations up to 200 spatial grid points were used, while 2D calculations were performed using a grid of 80×80 points. Simulations were mainly performed on a Silicon Graphics IRIS/Indigo R3000 workstation.

5.1. *1D structures*

Let us consider equation (1) in the case of one transverse dimension x, i.e. with $\nabla_\perp^2$ replaced by $\partial^2/\partial x'^2$. The results of the linear stability analysis of the transversely homogeneous stationary solution is identical to that of the 2D case and the Turing instability leads in 1D to the bifurcation of a spatially modulated solution which may be stable, whereas the corresponding roll pattern in 2D is always unstable against the onset of a hexagonal pattern, as we saw in Sections 3 and 4. More precisely, the analysis of [9] has shown that the bifurcation is supercritical, and hence the bifurcated solution is stable, for $\theta < 41/30$, whereas it is subcritical when

$$\theta > 41/30. \tag{38}$$

Let us now focus on the subcritical case in which, even if the modulated solution which bifurcates at the instability threshold is unstable, there exists a stable brach of modulated solutions which is disconnected from the homogeneous stationary solution and coexists with it in a suitable range of input field amplitude values E_I. Figure 11(a) shows an example of this situation for $\theta = 1.7$. The stable (unstable) part of the steady-state curve of the homogeneous stationary solution is shown by a full (broken) line. The dots represent the maximum and minimum values of the real part of the field amplitude in the stable

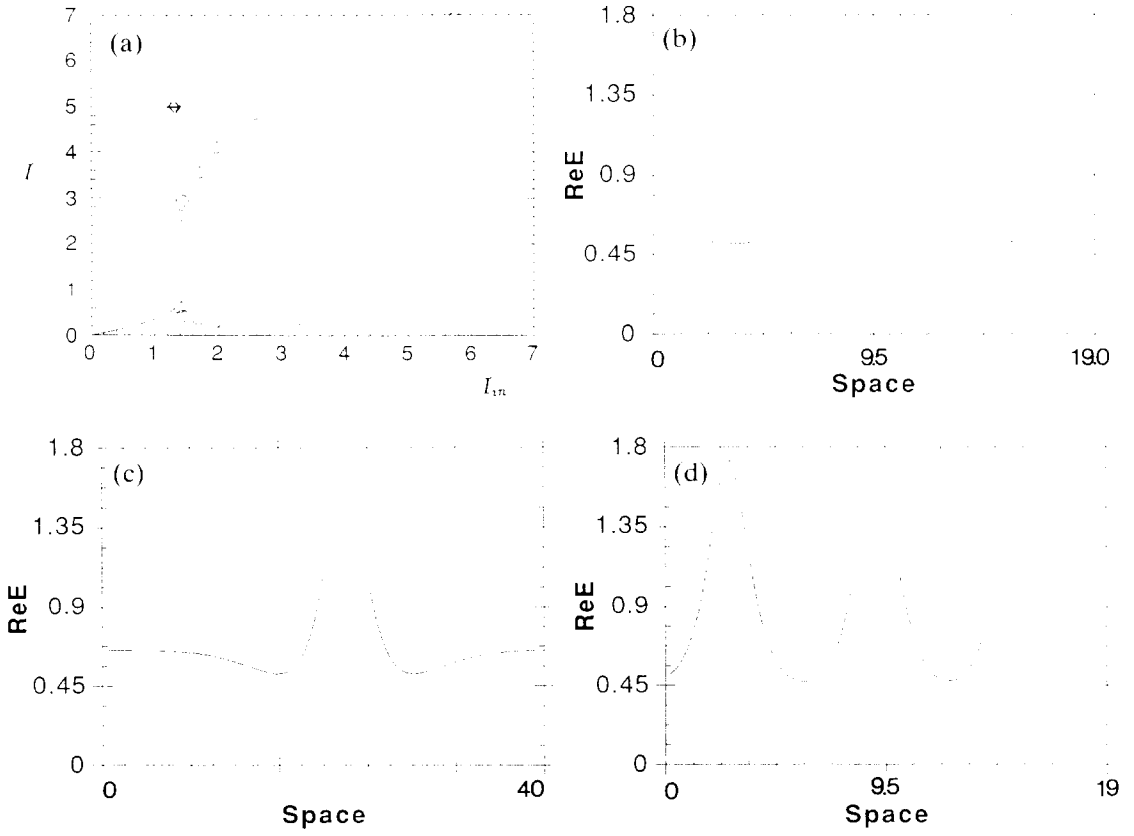

Fig. 11. (a) Steady-state curve of the homogeneous stationary solution for $\theta = 1.7$. The solid (broken) part is stable (unstable) against inhomogeneous perturbations. The dots indicate the maximum and the minimum value of $|E|^2$ of the modulated stationary solution in 1D. The arrows identify the interval of E_I in which the homogeneous and the modulated states coexist. (b) and (c) Localized structures in 1D for $E_I = 1.2$. (d) Modulated stationary solution in 1D for $E_I = 1.2$.

modulated pattern. The arrows indicate the interval of E_I where the modulated solution coexists with a stable homogeneous state. The profile of the modulated state is shown in Fig. 11(d) for $E_I = 1.2$. The localized structures can be found in the interval of E_I where the homogeneous and the modulated states coexist. An example is given in Fig. 11(b) for $E_I = 1.2$; it shows that the localized structures 'connect' the homogeneous and the modulated solution, in the sense that they are similar to one or the other solution in different spatial domains. In fact the height of the peak is exactly equal to the maximum value of the modulated state, while far from the peak the value of the field coincides with that of the homogeneous stationary state for the same value of E_I. Figure 11(c) shows the same state for a larger computational box, thus proving that this solution is independent of its size and from boundary effects. We note that, because the system has translational symmetry, each stationary solution (both of modulated and of localized nature) corresponds, in fact, to an infinity of stationary solutions obtained one from another by arbitrary translations along the x-axis. In addition, there are other localized stationary states which may display two, three or more isolated peaks, all with the same height equal to the maximum of the modulated solution while the value of the field far from one peak is equal to that of the homogeneous state.

Thus, there is a very large number of coexisting states: the homogeneous and the modulated states, and the localized solutions which connect them. The system approaches one or another according to the initial condition; for example, an initial spatial profile which presents a point-like peak of height comparable to the maxima of the modulated solution, evolves toward a localized stationary state centered at the position of the initial peak.

Figure 12(a) shows the same phenomena for a larger value of $\theta(\theta = 3)$, so that the steady-state curve of the homogeneous stationary solution is S-shaped. In this case the coexistence region is much more extended. Figures 12(b) and (c) exhibit a localized structure solution for $E_I = 1.6$ and $E_I = 2.0$, respectively. It can be noted that the peak height grows, with E_I following the maximum value of the modulated solution, shown in Fig. 12(d) for the same value of E_I as in Fig. 12(b).

These results can be linked to early work on spatial patterns in dispersive OB by Moloney *et al.* [40], in a model based on a mapping for longitudinal propagation, and mainly using Gaussian beam input. Moloney *et al.* [40] showed that the mapping tends towards the nonlinear Schrödinger equation in the limit of high finesse, as does equation (1). The localized structure can thus be interpreted as a soliton-like solitary wave. McDonald and Firth [41] later demonstrated that isolated 'solitons' could be created by address pulses, and were quasi-stable with plane-wave pumping but tended to coalesce when created on a Gaussian beam.

It must be noted that the modulated solution is stationary only up to a certain value of E_I (in the case of Figs. 11(a) and 12(a) this value is 2.4 and 2.5, respectively). Beyond this value the field profile enters a dynamical regime. More precisely, the system displays at first a periodic regime where the peaks oscillate more or less regularly; Fig. 13 shows these oscillations for $\theta = 3$, $E_I = 4$. The transverse coordinate x lies on the horizontal axis and time on the vertical axis. The value of $\mathrm{Re}(E)$ is measured by the grey scale; large (small) values correspond to lighter (darker) hues. The figure shows an antiphase oscillation of the adjacent peaks. The linear stability analysis of the homogeneous stationary solution does not predict any oscillatory instability [9]; these oscillations arise from a secondary bifurcation which affects the modulated solution.

If the input field is further increased, the system enters a complex spatio–temporal regime. The actual values of E_I corresponding to the above-mentioned dynamical instability thresholds is still not very well determined, because such thresholds proved to be

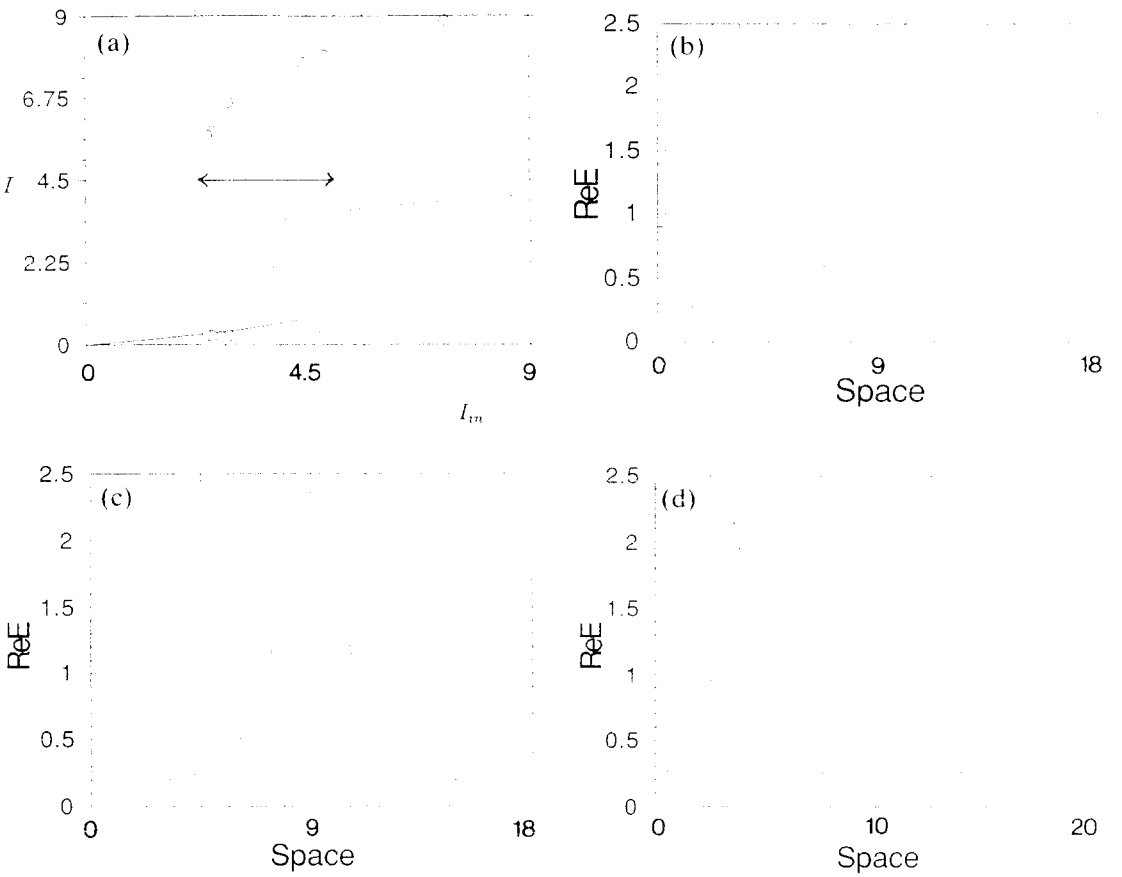

Fig. 12. (a) Same as Fig. 11(a), but for $\theta = 3$; (b) and (c) localized structures in 1D for $E_I = 1.6$ and $E_I = 2$, respectively; (d) modulated stationary solution in 1D for $E_I = 1.6$.

dependent on the transverse size of the system; this means that using a spatial computational lattice of, e.g. 100 points, the simulations will display the onset of the temporal oscillations for a value of E_I smaller than one could find when using a lattice of, e.g. 200 points. This is a mark of the relevance of boundary conditions in such phenomena.

5.2. *2D simulations*

In the case of two transverse dimensions, the localized structures are met in the same domain of E_I where, in the 1D case the homogeneous stationary solution coexists with the modulated solution as a consequence of a subcritical bifurcation. In 2D, however, the homogeneous state coexists with a hexagonal pattern, because the roll pattern which corresponds to the 1D modulated solution is unstable.

Figure 14 displays some structures obtained for $\theta = 1.7$ and $E_I = 1.2$; the quantity shown is again $\mathrm{Re}(E)$ in the transverse plane. In particular Fig. 14(a) exhibits the hexagonal pattern, where some local defects can be identified. Figure 14(b)–(d) show 2D localized structures with one, two and three dots, respectively: here the dots of maximum $\mathrm{Re}(E)$ are such that their value is the same as in the peaks of the hexagons in Fig. 14(a), while in the rest of the transverse plane, $\mathrm{Re}(E)$ has the same value as in the homogeneous stationary

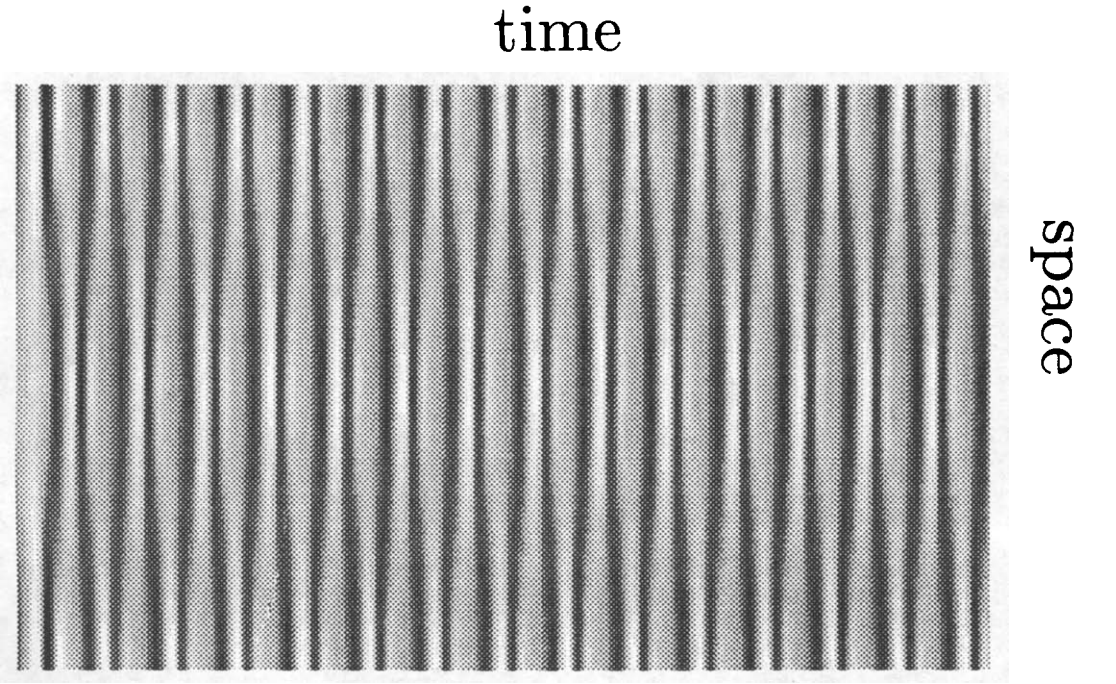

Fig. 13. Regular oscillations in the 1D modulated solution for $\theta = 3$, $E_I = 4$. The horizontal axis corresponds to the spatial variable x, the vertical axis corresponds to the time variable.

solution. Figure 14(e) shows a single hexagon with seven dots; finally in Fig. 14(f) the homogeneous state is present in the upper and lower portion of the transverse plane, while the central part displays a hexagonal structure identical to that of Fig. 14(a) (some defects at the boundary are visible). All the results we showed for the localized structures hold in the self-focusing case $\eta = 1$ both in 1D and 2D. In the case of self-defocusing ($\eta = -1$) research is in progress, but has not evidenced localized states in 2D.

The existence of the localized structures seems very interesting from the optical information processing viewpoint. The intensity peaks in these states can work as pixels, and the possibility of having a large number of them, and of locating them at arbitrary positions (and possibly of shifting them) is interesting. Of course, it is crucial to assess (1) the possibility of controlling the pixels, in the sense of writing and erasing arbitrarily the localized dots (e.g. using appropriately spatially modulated input beams), and (2) the limitation in density and positioning of the dots. These problems have been addressed in the 1D 'mapping' case by the Strathclyde group [41, 42]. Their adaptation to the mean-field model and to 2D will be the subject of future work.

6. GAUSSIAN PUMP

The analysis and simulations of Sections 3 and 4 treat the case where the external pump field, parameterized by E_I in equation (1), is a plane-wave. This enables us to obtain quantitative analytical predictions which we can compare with the results of simulations. In an experiment, however, the pump will have a variation, probably Gaussian in shape, in the plane transverse to the direction of propagation. This section, then, attempts to address the more realistic case where the pump field has a Gaussian transverse profile.

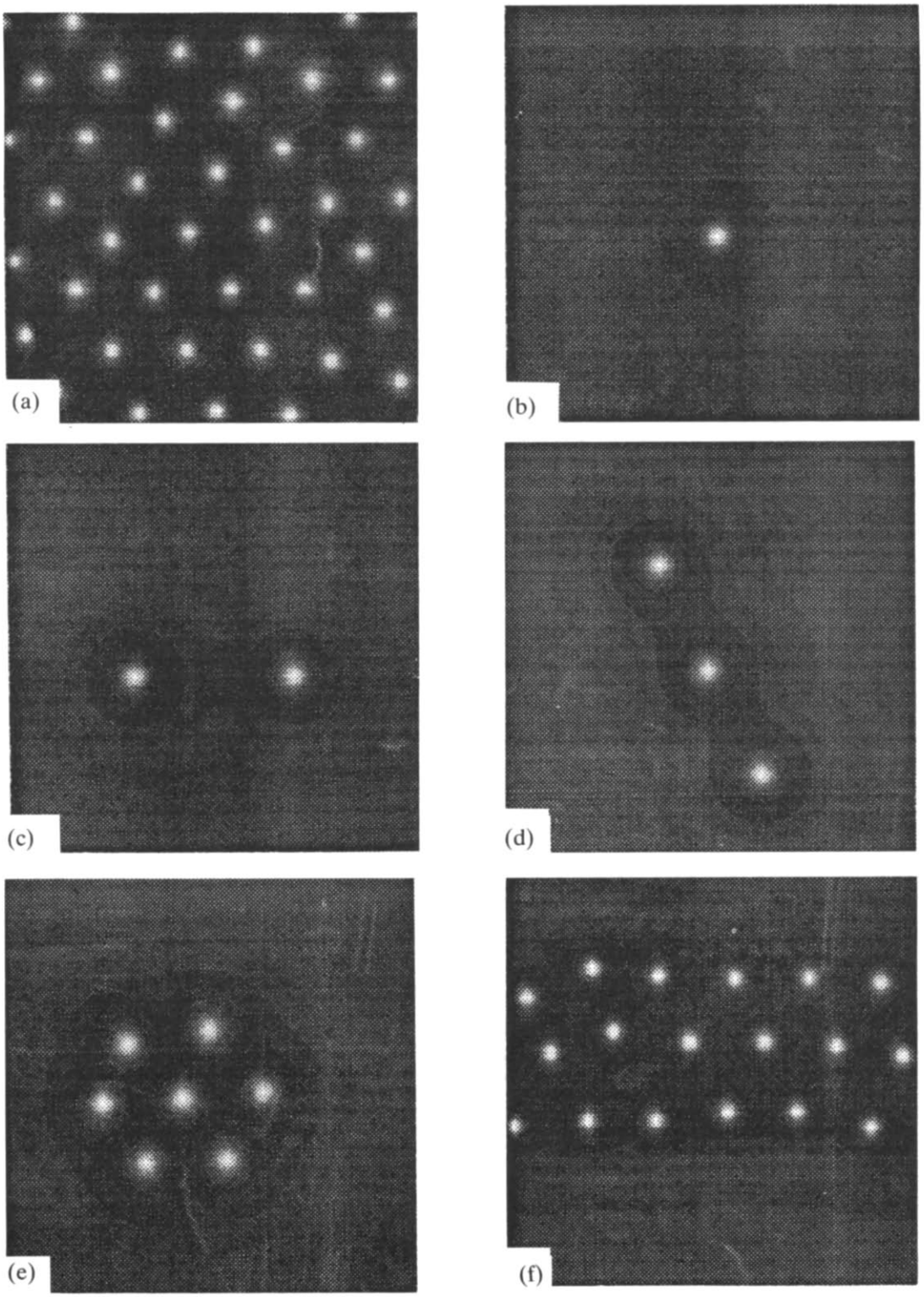

Fig. 14. Patterns and localized structures in 2D. (a) Hexagonal pattern; (b), (c), (d) one, two and three-dot localized solutions, respectively; (e) single hexagon; (f) stripe of hexagons.

An examination of the derivation of the mean-field model [9] shows that we are free to regard E_I in equation (1) as a function of the transverse coordinates so long as the spatial extent of this function is larger than the scale of the pattern. This function should represent the transverse variation of the pump field at the entrance to the nonlinear medium.

With this in mind, equation (1) can now be used with the constant E_I replaced by a function of the transverse coordinates of the of form $E_I \exp(-r^2/\omega_0^2)$ where $r^2 = x^2 + y^2$ and ω_0 is the waist of the pump beam, which acts as a control parameter in addition to the pump amplitude E_I.

With a Gaussian source term in equation (1) we can no longer perform a linear stability analysis, since we are unable to determine analytically the zero-order solution around which to do the analysis. It is possible to predict the kind of solution which may emerge from any symmetry-breaking bifurcation, however, from considerations of the symmetry of the full problem (equation plus boundary conditions), as has been demonstrated recently for the case of a Kerr slice with single feedback mirror [43]. With Gaussian pump beam the symmetry of the problem corresponds to the O_2 group, rather than to the Euclidean group E_2 of the plane-wave pump case. This means that the constraint of bifurcation to patterns with discrete translational symmetries is no longer applicable, i.e. we are not restricted to patterns which will tile the plane. We may then expect solutions with polygonal patterns of spots corresponding to the subgroups D_n of O_2, rather than the hexagons of the plane-wave case.

We have integrated equation (1) with a Gaussian pump using a modified version of the Hopscotch code used for the plane-wave simulations described in Section 4. A square grid of 128×128 points was generally used, with the integration now being carried out on a circular domain within the square grid. We discuss first of all the case of a self-focusing medium and concentrate on results obtained for $\theta = 0$. We find that the lowest order solution depends only on the radial coordinate r and thus shows the full O_2 symmetry. By altering the control parameters ω_0 and E_I we observe bifurcations to steady-state patterns with dihedral symmetry D_n with $n = 2, 3, 5, 6$, the patterns with larger n generally being obtained for larger pump waists (see Figs 15–19).

In Figs 5, 6, 9 and 10 we displayed only the near-field pattern, i.e. the spatial configuration of the field E in the cavity or in the immediate neighbourhood of the cavity. In Figs 15(b)–20(b) we also show the far-field configuration, which corresponds to the Fourier transform of the near-field. As done, for example, in the experiments of [24], we remove the central zero-frequency spot. As a comparison with the small aspect ratio simulations used to produce Figs 15–19, Fig. 20 shows the pattern obtained from a simulation performed with a relatively large value of pump waist ($\omega_0 = 21.972$) on a 512×512 point grid. The field displays hexagonal structures reminiscent of the plane-wave pump case. The threshold value of the pump intensity necessary for an instability of the basic state varies smoothly with the size of the pump waist ω_0, starting off close to the plane-wave threshold for large pump waists and increasing as the width of the pump is decreased. In principle, approximations to threshold curves in the (ω_0^2, E_I)-plane for each pattern are obtainable numerically. In regions where two such curves seem to approach each other metastability of patterns can sometimes be seen: one pattern forms from noise and persists for times of the order of 100 or 200 cavity lifetimes, after which the other pattern forms and appears to be stable; that is, it lasts until the end of the simulation, which is usually about 1600 cavity lifetimes long. Bistability between patterns can also be seen. By starting from a stationary pattern and slowly increasing the pump waist it is possible to have this pattern stable in a region of the parameter space where a different pattern forms from noise. Secondary bifurcations from the triangular and 'rhomboidal' patterns obtainable at small values of the pump waist can be seen when the pump

amplitude is increased sufficiently: the stationary patterns begin to rotate, the only type of secondary bifurcation expected from a solution with symmetry D_n where n is prime [43].

With D_6 (hexagonal) patterns we have also observed the kind of behaviour reported in [43]. We have seen secondary bifurcations to solutions with symmetry D_2 followed by irregular itinerancy among patterns with imperfect D_3, D_2 and D_6 symmetry. Simulations for values of $\theta \neq 0$ have shown the same qualitative results as in the $\theta = 0$ case, with the length scale of the pattern generally increasing with θ, as predicted analytically and observed numerically in the plane-wave case. For the case of a defocusing medium we have been unable to observe any symmetry-breaking bifurcations for any of the parameter values tried. There is, therefore, agreement with the plane-wave case where we also see no stationary transverse patterns.

7. CONCLUSIONS

In this paper we have given a description of pattern formation in a high-finesse Kerr cavity. This, the dispersive limit of the standard mean-field model of optical bistability, ought to be amenable to experimental investigation.

We have found pattern formation only for a self-focusing medium, which conforms to the intuitive picture of nonlinearity being able to compensate diffraction only on the self-focusing side. For a plane-wave (i.e. broad) pump, we find hexagon formation in the simulations, with amplitudes in reasonable conformity with the results of two forms of nonlinear analysis of the model. Both analyses and simulations point to the existence of a region of coexistence of stable hexagons and stable plane-wave solutions—i.e. the bifurcation is transcritical. The general behaviour is similar to that observed in other spheres, e.g. in fluid convection [1]. The intrinsically two-dimensional nature of the hexagonal structures, as well as the coexistence phenomenon, demonstrates that one-dimensional treatments have a validity restricted to situations where the second transverse dimension is physically suppressed.

Simulations well above threshold indicate a progression from stable regular patterns, through static defected patterns, to an apparently turbulent motion of a 'gas' of bright spots.

Under the conditions such that the 1D model predicts the subcritical bifurcation of a modulated pattern, one meets both in 1D and 2D interesting localized structures which connect the homogeneous state with the modulated solution in the interval of input field values where the two states coexist. The scenario we find here is similar to that uncovered in the case of nonlinear chemical reactions [35] and of hydrodynamics [36]. The flexibility of these localized states, in terms of number and position of the intensity peaks, make these results interesting also from the viewpoint of possible applications to optical information processing.

The underlying optical bistability complicates the behaviour, particularly where the threshold intracavity intensity lies on or near the unstable branch of the characteristic. In particular, it frustrates the pattern formation for a self-defocusing medium. It should be noted, however, that for a self-focusing medium pattern formation occurs also in parts of the monostable regime.

With a view to experiment, simulations have been undertaken with a gaussian pump beam. The general behaviour is similar to that of the plane-wave pump, but with differences associated with the different symmetry of the two problems. An extension of the present treatment, again with a view to experiment, would include the possibility of curved mirrors, which would make a cavity mode description possible. Alternatively, one

can relax the dispersive limit, and consider a two-level medium, which has an absorptive as well as dispersive nonlinearity [28]: work on this problem will be reported elsewhere.

Finally, it is worth making a general observation on the physical origin of these instabilities. It was noted in Section 2 that the transverse wavevector and the cavity tuning parameter appear only in combination in the stability analysis. The form of this combination strongly suggests a physical interpretation, namely that the patterns arise because off-axis waves can compensate the mistuning of the cavity and attain cavity resonance. This suggests a rather general mechanism, and indeed such 'tilted-wave' resonances have been proposed in lasers [44] and in optical parametric oscillators [45], as well as the present passive cavity configuration.

Acknowledgements—We are grateful to M. Brambilla for his continuous help. We would like to thank P. Mandel, M. Taki and O. Lejeune for helpful interactions. We would also like to thank G. K. Harkness for help with the preparation of some of the figures. This work is supported by the EC via ESPRIT grant 7118 (TONICS), by Science and Engineering Council Grant GR/G 12665, by the NATO collaborative research grant n. 921142 and by the CNR Research grant 92.01369.CT02. AJS acknowledges support from a SERC Studentship.

REFERENCES

1. G. Nicolis and I. Prigogine, *Self-Organization in Non Equilibrium Systems*. Wiley, New York (1977).
2. H. Haken, *Synergetics—An Introduction*. Springer, Berlin (1977).
3. A. M. Turing, The physical basis of morphogenesis, *Phil. Trans. R. Soc.* **B237**, 37 (1952).
4. N. B. Abraham and W. J. Firth, editors. Special issues on Transverse effects in nonlinear optical systems, *J. Opt. Soc. Am.* **B7** (6, 7), (1990).
5. L. A. Lugiato, Spatio-temporal Structures-Part I, in Proc. Solvay Conference on Quantum Optics, edited by P. Mandel, *Phys. Rep.* **219**, 293–310 (1992).
6. C. O. Weiss, Spatio-temporal Structures. Part II, in Proc. Solvay Conference on Quantum Optics, edited by P. Mandel, *Phys. Rep.* **219**, 311–338 (1992).
7. J. V. Moloney and H. M. Gibbs, Role of diffraction coupling and self-focusing or defocusing in the dynamical switching of a bistable optical cavity, *Phys. Rev. Lett.* **48**, 1607–1609 (1982); J. V. Moloney, H. Adachihara, D. W. McLaughlin and A. C. Newell, in *Chaos, Noise and Fractals*, edited by R. Pike and L. A. Lugiato. Hilger, Bristol (1988); J. V. Moloney and A. C. Newell, *Nonlinear Optics*, Addison Wesley, Reading, HA (1992).
8. J. V. Moloney, H. Adachihara, R. Indik, C. Lizaragga, R. Northcutt, D. W. McLaughlin and A. C. Newell, Modulational-induced optical pattern formation in a passive optical-feedback system, *J. Opt. Soc. Am.* **B7**, 1039 (1990).
9. L. A. Lugiato and R. Lefever, Spatial dissipative structures in passive optical systems, *Phys. Rev. Lett.* **58**, 2209–2211 (1987).
10. I. Prigogine and R. Lefever, Symmetry breaking instabilities in dissipative systems—II, *J. Chem. Phys.* **48**, 1695–1700 (1968).
11. H. M. Gibbs, S. L. McCall and T. N. C. Venkatesan, Differential gain and bistability using a sodium filled Fabry–Pérot interferometer, *Phys. Rev. Lett.* **36**, 1135–1138 (1976).
12. G. Grynberg, E. Le Bihan, P. Verkerk, P. Simoneau, J. R. R. Leite, D. Bloch, S. Le Boiteux and M. Ducloy, Observation of instabilities due to mirrorless four-wave mixing oscillation in sodium, *Opt. Comm.* **67**, 363 (1988).
13. W. J. Firth and C. Paré, Transverse modulational instabilities for counterpropagating beams in Kerr media, *Opt. Lett.* **13**, 1096–1098 (1988).
14. G. Grynberg and J. Paye, Spatial instability for a standing wave in a nonlinear medium, *Europhys. Lett.* **8**, 29 (1989).
15. J. Pender and L. Hesselink, Degenerate conical emission in atomic-sodium vapor, *J. Opt. Soc. Am.* **B7**, 1361 (1990).
16. G. Grynberg, Mirrorless four-wave mixing oscillation in atomic vapors, *Opt. Comm.* **66**, 321 (1988).
17. W. J. Firth, Spatial instabilities in a Kerr medium with single feedback mirror, *J. Mod. Opt.* **37**, 151 (1990); G. D'Alessandro and W. J. Firth, Spontaneous hexagon formation in a nonlinear optical medium with feedback mirror, *Phys. Rev. Lett.* **66**, 2597–2600 (1991); G. D'Alessandro and W. J. Firth, Hexagonal pattern formation for a Kerr slice with a feeback mirror, *Phys. Rev. A*, **46**, 537 (1992).
18. M. Tamburrini, M. Bonavita, S. Wabnitz and E. Santamato, Hexagonally patterned beam filamentation in a thin liquid-crystal film with a single feedback mirror, *Opt. Lett.* **18**, 855 (1993); E. Ciaramella, M. Tamburrini and E. Santamato, *Appl. Phys. Lett.* (1993).
19. R. McDonald and H. J. Eichler, Spontaneous optical pattern formation in a nematic liquid crystal with feedback mirror, *Opt. Comm.* **89**, 289–295 (1992).
20. T. Honda, Hexagonal pattern formation due to counterpropagation in KN_6O_3, *Opt. Lett.* **18**, 598–600 (1993).

21. G. Grynberg, private communication.
22. J. Y. Courtois and G. Grynberg, Spatial pattern formation for counterpropagating beams in a Kerr medium: a simple model, *Opt. Comm.* **87**, 186–192 (1992).
23. R. Chang, W. J. Firth, R. Indik, J. V. Moloney and E. M. Wright, Three-dimensional simulations of degenerate counterpropagating beam instabilities in a nonlinear medium, *Opt. Comm.* **88**, 167 (1992).
24. A. Petrossian, M. Pinard, A. Maitre, J. Y. Courtois and G. Grynberg, Transverse pattern formation for counterpropagating laser beams in rubidium vapor, *Europhys. Lett.* **18**, 689–694 (1992).
25. See e.g., S. Chandrasekhar, *Hydrodynamics and Hydrodynamics Stability*. Clarendon Press, Oxford (1961).
26. W. J. Firth, A. J. Scroggie, G. S. McDonald and L. A. Lugiato, Hexagonal patterns in optical bistability, *Phys. Rev.* **A46**, R3609 (1992).
27. P. Manneville, *Dissipative Structures and Weak Turbulence*. Academic Press, San Diego (1990).
28. L. A. Lugiato and C. Oldano, Stationary spatial patterns in passive optical systems: Two-level atoms, *Phys. Rev.* **A37**, 3896 (1988); L. A. Lugiato, Wang Kaige and N. B. Abraham, Spatial pattern formation and instabilities in passive nonlinear resonators, unpublished.
29. M. Haelterman, M. Tolley and G. Vitrant, Transverse effects in optical bistability with the nonlinear Fabry–Pérot étalon, *J. Appl. Phys.* **67**, 2725–2730 (1990); M. Haelterman, G. Vitrant and R. Reinisch, *J. Opt. Soc. Am.* **B7**, 1309 (1990); M Haelterman, The role of diffraction in optical bistability with the nonlinear Fabry–Pérot: A pole analysis, *Opt. Comm.* **75**, 165–167 (1990).
30. L. A. Lugiato and F. Castelli, Quantum noise reduction in a spatial dissipative structure, *Phys. Rev. Lett.* **68**, 3284–3286 (1992).
31. S. Ciliberto, P. Coullet, J. Lega, E. Pampaloni and C. Perez-Garcia, Defects in roll hexagon competition, *Phys. Rev. Lett.* **65**, 2370–2373 (1990).
32. A. R. Gourlay, *J. Inst. Math. Applic.* **6**, 375 (1970); A. R. Gourlay, G. R. MacGuire, *J. Inst. Math. Applic.* **7**, 216 (1971).
33. R. H. Hardin and F. D. Tappert, *SIAM Rev.* **15**, 423 (1973).
34. S. Trillo and S. Wabnitz, Dynamics of the nonlinear modulational instability in optical fibers, *Opt. Lett.* **16**, 986–988 (1991).
35. S. Koga and Y. Kuramoto, Localized patterns in reaction–diffusion systems, *Progr. Theor. Phys.* **63**, 106–121 (1980); V. Hahim, P. Jakobsen and Y. Pomeau, Fronts vs. solitary waves in nonequilibrium systems, *Europhys. Lett.* **11**, 19–24 (1990); G. Dewel and P. Borckmans, in *Far from Equilibrium Dynamics in Chemical Systems*, edited by S. Popielanski and J. Gorecki, p. 83. World Scientific, Singapore (1991).
36. S. Toh, H. Iwasaki and T. Kawahara, Two-dimensionally localized pulses of a nonlinear equation with dissipation and dispersion, *Phys. Rev.* **A40**, 5472 (1989); O. Thual and S. Fauve, Localized structures generated by subcritical instabilities, *J. Phys. (France)* **49**, 1829–1833 (1988); A. V. Gaponov-Grekhov, A. S. Lomov, G. V. Osipov and M. I. Rabinovich, in *Nonlinear Waves* Vol. 1, edited by A. V. Gaponov-Grekhov, M. I. Rabinovich and I. Engelbrecht, p. 65. Springer, Heidelberg (1989).
37. M. Tlidi, P. Mandel and R. Lefever, Localized structures and localized patterns in optical bistability, submitted for publication.
38. M. Tlidi and P. Mandel, Spatial patterns in nascent optical bistability, *Chaos, Solitons & Fractals* **4**(8/9), (1994).
39. M. Tlidi, M. Georgiou, P. Mandel, Spatial patterns in nascent optical bistability, *Phys. Rev.* **A48**, 4605 (1993).
40. D. W. McLaughlin, J. V. Moloney and A. C. Newell, Solitary waves as fixed points of infinite dimensional maps in an optically bistable ring cavity, *Phys. Rev. Lett.* **51**, 75–78 (1983).
41. G. S. McDonald and W. J. Firth, Spatial solitary-wave optical memory, *J. Opt. Soc. Am.* **B7**, 1328 (1990); G. S. McDonald and W. J. Firth, Switching dynamics of spatial solitary wave pixels, *J. Opt. Soc. Am.* **B10**, 1081–1089 (1993).
42. K. D. Stephen, Ph.D. thesis, Strathclyde University, Glasgow (1991).
43. F. Papoff, G. D'Alessandro, G. L. Oppo and W. J. Firth, Local and global effects of boundaries on optical pattern formation in Kerr media, *Phys. Rev.* **A48**, 634 (1993).
44. P. K. Jakobsen, J. V. Moloney, A. C. Newell and R. Indik, Space–time dynamics of wide-gain-section lasers, *Phys. Rev.* **A45**, 8129–8137 (1992).
45. G.-L. Oppo, M. Brambilla and L. A. Lugiato, Formation and evolution of roll patterns in optical parametric oscillators, *Phys. Rev.* **A**, in press.